Design and Fabrication of Laminated CoZrTaB Magnetic Core Inductor

by

Yanze Wu

A Dissertation Presented in Partial Fulfillment
of the Requirements for the Degree
Doctor of Philosophy

Approved July 2022 by the
Graduate Supervisory Committee:

Hongbin Yu, Chair
Shamala Chickamenahalli
Nicholas Rizzo
Michael Goryll

ARIZONA STATE UNIVERSITY

August 2022

ABSTRACT

The strong demand for the advancing of Moore's law on device size scaling down has accelerated the miniaturization of passive devices. Among these important electronic components, inductors are facing challenges because the inductance value, which is strongly dependent on the coil number for the air core inductor case, will be sacrificed when the size is shrinking. Adding magnetic core is one of the solutions due to its enhancement of inductance density but it will also add complexity to the fabrication process, and the core loss induced by the eddy current at high frequency is another drawback.

In this report, the output of this research will be presented, which has three parts. In the first part, the CoZrTaB thin films are sputtered on different substrates and characterized comprehensively. The laminated CoZrTaB thin films have been also investigated, showing low coercivity and anisotropy field on both Si and polyimide substrates. Also, the different process conditions that could affect the magnetic properties are investigated.

In the second part, Ansys Maxwell software is used to optimize the lamination profile and the magnetic core inductor structure. The measured M-H loop is imported to improve the simulation accuracy.

In the third part, a novel method to fabricate the magnetic core inductors on flexible substrates is proposed. The sandwich magnetic core inductor is fabricated and assembled with flipchip bonder. The measurement result shows that this single-turn magnetic core inductor can achieve up to 24% inductance enhancement and quality factor of 7.42. The super low DC resistance (< 60 mΩ) proves that it is a good candidate to act as the passive

component in the power delivery module and the use of polyimide-based substrate extends its compatibility to more packaging form factors.

DEDICATION

To my family, with Love.

ACKNOWLEDGMENTS

I would like to express my most sincere gratitude to my committee chair, Professor Hongbin Yu, who has devoted continuous support, and patience during my PhD study. He has accepted me as a member of his group since 2018 spring and since then, he has opened the door of research for me. He used his wisdom, experience, and knowledge to inspire me to keep overcoming difficulties, learning new technologies, and pushing this project moving forward. Also, his management over the whole group, which has students from different backgrounds and working for different projects, encourages me to be a researcher with positive spirits, good leadership, and modest attitude.

I would like to thank my committee members, Professor Shamala Chickamenahalli, Professor Michael Goryll, and Dr. Nicholas Rizzo for providing guidance and helpful discussions. In particular, Professor Michael Goryll helped me finish the device assembly step with his flip-chip bonding machine; and Dr. Nicholas Rizzo helped our group set up the SHB-looper, which takes a lot of time and efforts.

I would like to thank members past and present of Dr. Hongbin Yu's group for their help and support, especially Dr. Jignesh Vanjaria and Dr. Todd Houghton, who have taught me a lot about material characterization.

I would like to thank all of the staff at ASU Nanofab and Goldwater Materials Science Facility for their patient and professional training services.

Finally, but most importantly, I would like to thank my parents for their unstoppable caring, support, and love through my life so far. I am always feeling accompanied even if they are in another country now, and the connection is stronger than ever.

TABLE OF CONTENTS

Page

CHAPTER Page

LIST OF TABLES

Table Page

LIST OF FIGURES

Figure Page

Figure Page

Figure Page

CHAPTER 1

INTRODUCTION

1.1 Motivation

Currently, the trend to miniaturize the passive components has been boosted by the development of semiconductor industry, including the new packaging technology, the scaling down of the devices, and the emerging application scenarios. For example, the in-package air core inductor (ACI) was used for the Fully Integrated Voltage Regulator (FIVR) module, starting from Intel's 22nm node CPUs (Haswell).[1] Owing to the relatively large footprint and thick substrate, the ACIs had a high quality factor in the beginning, which, however, would be challenged because of the shrinking footprint and the thinner substrate core. Most of the parameters of ACIs, such as the inductance, DC resistance (RDC), are proportional to the number of coils, and trace width, respectively, suggesting a severe performance drop as the chip size continues to scale down. The magnetic inductor array (MIA) was first introduced in the 10th generation Intel CPUs (14 nm node), with an iron-alloy based nanoparticle (NP) mixed in epoxy matrix being used as magnetic core, of which the inductance is 2.5-3.0 nH.[2] Compared with ACIs, the MIAs take about half of the area and the thickness is below 180 μm. Moreover, the coaxial magnetic integrated inductor (Coax MIL) is also under development for the 12^{th} generation Intel CPUs (10 nm node), which is directly fabricated in the plated through hole (PTH) in the substrate core layer with a straight Cu trace surrounded by the magnetic core, which requires smaller footprint and is more suitable for mobile CPUs.[3]

The other application, automotive electronics, places emphasis on footprint/size, integration compatibility, and mechanical stability. Details of the latter two factors are

different from the cases in the Intel's examples. The working condition requires the substrate material to be more durable under high temperature and wide-range vibration, indicating that more complex packaging form like heterogeneous packaging has to be considered.[4] Under this circumstance, integration compatibility with polyimide, FR4, or even ceramic materials is important to the passive components.[5] For instance, an embedded inductor in eWLB (Embedded Wafer Level Ball Grid Array) package is able to better suppress the voltage-controlled oscillator (VCO) phase noise, compared with the on-chip inductor, directly elevating the integration density and the system performance of the automotive radar transceiver module.[6]

In the two applications that have been mentioned above, the demand for die size scaling and the substrate thickness shrinking has put the air core inductor in a dilemma because the inductance and RDC would deteriorate and further affect the quality factor or efficiency of the whole module. Adding the magnetic core is a solution to improve the inductance deterioration (such as Intel's MIA, MIL),[2, 3] but the additional integration complexity cannot be ignored. Also, the selection of the magnetic materials also affects the integration compatibility with the substrate materials. Metallic NP mixed in epoxy matrix has been implemented due to its low deposition difficulty. However, the permeability of these materials is relatively low (less than 10) and the inductance enhancement is limited.[3] Another option is to use the sputtered alloys, which have a much higher permeability, but the substrate requirement for the sputter process is stricter.[7] Also, the stacking of the different layers (magnetic core layers, Cu trace layers) has to be finished by multiple lithography process, which comes with several baking process and high cost.[8] So far,

each kind of topology of the Cu trace have been investigated intensively, such as spiral,[9, 10] solenoid,[11] and toroid[12], as shown in Fig.1.

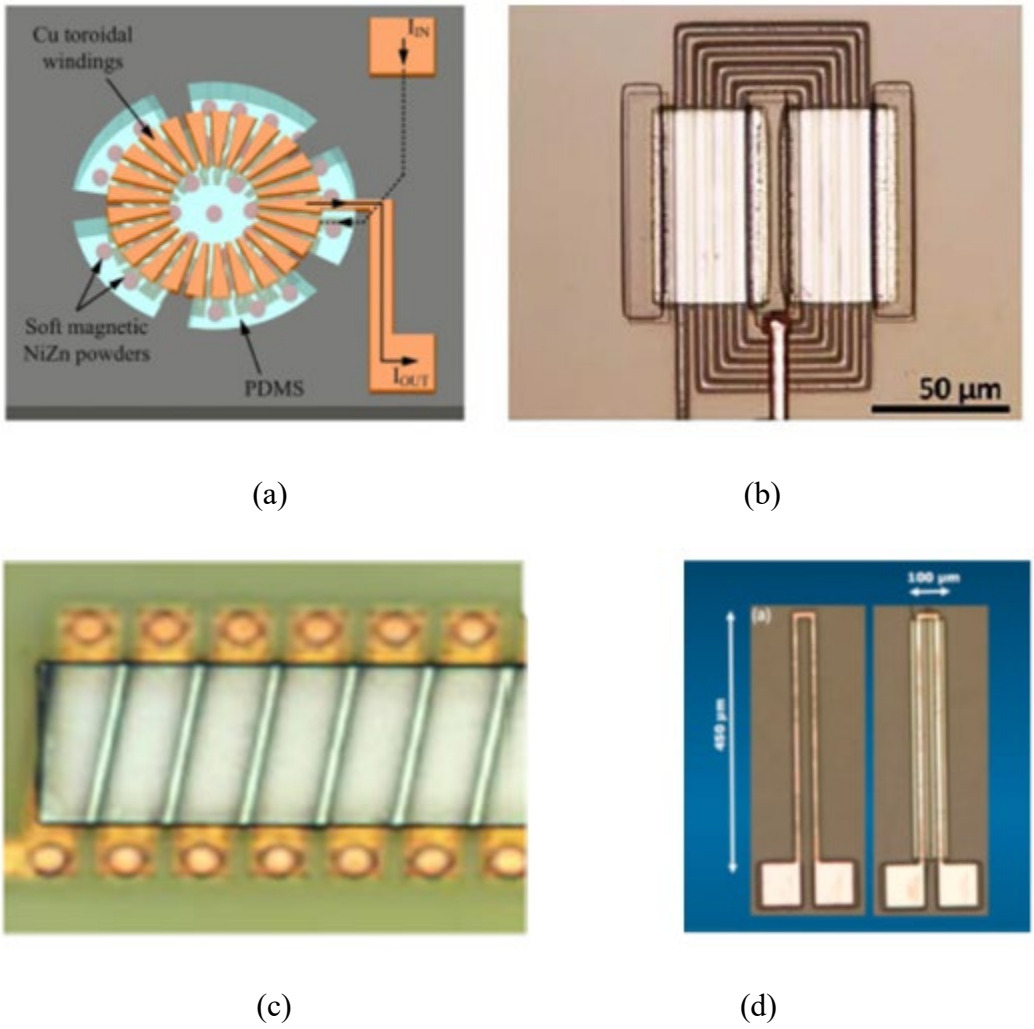

(a) (b)

(c) (d)

Fig. 1 Examples of inductors with different topologies. (a) toroid[12] (b) spiral[13] (c) solenoid[14] (d) strip-line[15].

Incorporated with the magnetic core, it has been reported [9-12] these inductors can achieve 30-100 nH when the frequency is lower than 100 MHz, nonetheless, the large device area (3-10 mm^2) and DC resistance (above 0.2 Ω) would result in difficulty to the integration into the power delivery module and sacrificing the efficiency ratings. Basically,

the total length of Cu trace required by the complicated topology and the interface of the Cu Via are responsible for the two issues mentioned above.[16] Under this circumstance, the straight line one-turn magnetic core inductor would be a solution to lowering the DC resistance and miniaturization. Some of magnetic core inductors from research or industry are listed in Table 1, including our group's previous results.

Table 1
Parameters of Some Magnetic Core Inductors (Frequency = 100 MHz)

Product Source	Core Material	Size (mm^2)	Inductance (nH)	DCR (mΩ)	ACR (Ω)
Swaminathan's group[17]	CIP	11.6	24.5	22.4	1.078
Dialog[18]	Not disclosed	1.5	5	20-50	Not disclosed
Sturcken's group[19]	Ni-Fe	0.245	8	270	3
Intel 3D-TSV inductor[20]	Not disclosed	0.0525	4.8	Not disclosed	Not disclosed
Yu's group spiral inductor[21]	CoZrTaB	0.014	6	Not disclosed	4.18
Yu's group strip-line inductor[15]	CoZrTaB	0.045	3	Not disclosed	0.589

In this report, CoZrTaB thin film is investigated to achieve the best parameters; then we introduce a novel process method to fabricate the integration inductor with dual-layer magnetic core, which is an extension of the group's prior work on both rigid[13, 21] and organic substrates[22]. Basically, the inductor trace is made on a commercially available flexible PCB with a wet etch process, of which the thickness of Cu layer is 18 μm to obtain a low DC resistance. The magnetic core is fabricated by sputtering and patterned by a standard lift-off process, enabling its good compatibility with the semiconductor process used in industry. In the device assembly step, the flipchip bonder was utilized, providing a fast and well-aligned bonding. The following RF/DC measurement results show that the magnetic core can effectively increase the inductance by up to 24%, while it can still keep the low-profile form factor, low DC resistance (< 60 mΩ) and the finished device shows great flexibility and provides a good potential for the integration into various package forms.

1.2 Organization

Following this chapter, Chapter 2 starts with introduction of fundamentals of the magnetization process, including the details of significant parameters and the requirement in our research. Then the optimization of the CoZrTaB magnetic thin film properties is discussed.

In Chapter 3, the laminated CoZrTaB thin film is further investigated and the design of an air core/magnetic core inductor is improved using Ansys Maxwell simulation software.

Chapter 4 introduces a method to fabricate the inductors designed in the previous chapter. The use of a flipchip bonder helps us fabricate a sandwich structure magnetic core inductor with only one sputter session of CoZrTaB thin film.

Chapter 5 introduces the DC/RF measurement system used in our lab and presents the measurement results of air core/magnetic core inductors that we fabricated in the ASU Nanofab. The measurement results show that the performance of fabricated inductors agrees with the simulation results. The DCR is as low as 49.8 $m\Omega$ and the inductance reaches 3.47 nH. Also, the use of a polyimide substrate makes it possible to be integrated in a wide range of packaging forms.

Chapter 6 is the conclusion of this research.

CHAPTER 2

MAGNETIC THIN FLIM CHRACTERIZATION AND OPTIMIZATION

2.1 Important Parameters and Fundamental Concepts

2.1.1 Magnetization[23, 24]

According to the quantum mechanics, magnetism can be explained as a "macro result" of the magnetic dipole moment of many individual atoms. When an external magnetic field (H, $\mathrm{A \cdot m^{-1}}$) is applied to the magnetic thin film, the initially random-oriented dipole moments (Fig. 2 (a) or (b)) will be re-arranged, with the result that each moment will align with each other and the net magnetization will increase. Eventually, all the dipoles are in the same direction when the external field is large enough, as shown in Fig. 2 (d). This process is called magnetization.

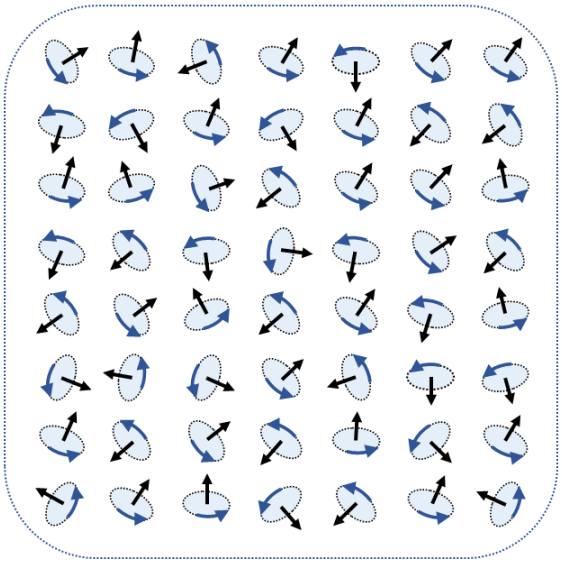

(a)

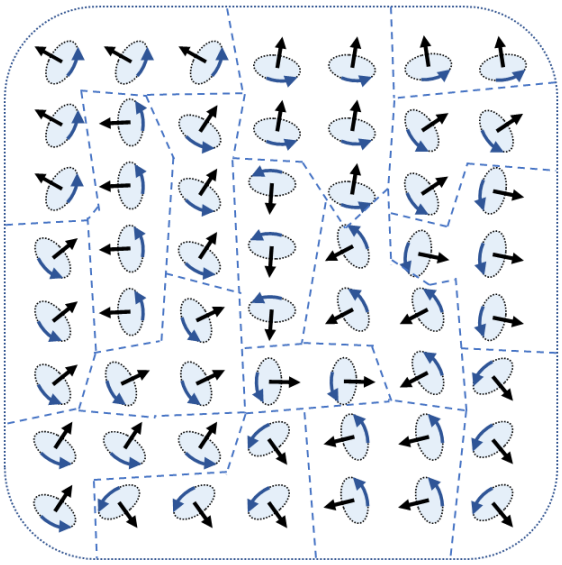

(b)

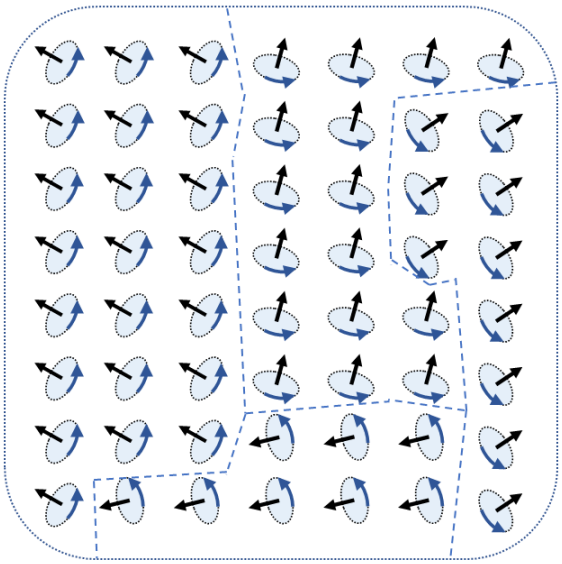

(c)

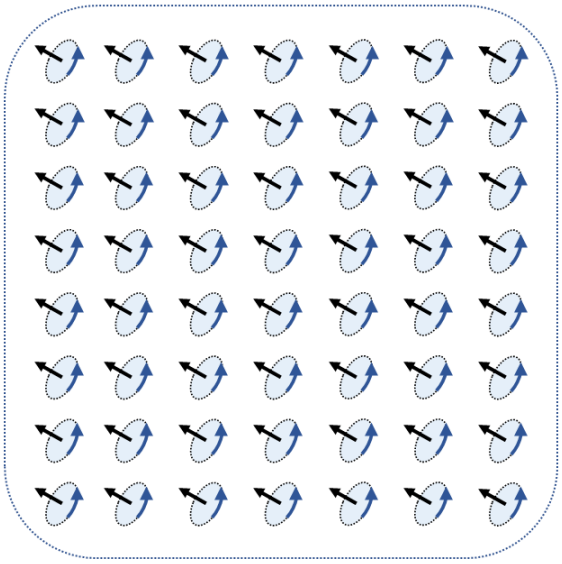

(d)

Fig. 2 Schematic of the magnetization process. (a) initial state of a bulk paramagnetic material without applied field (b) initial state of a bulk ferromagnetic material without applied field (c) magnetic domains begin to merge when the applied field increases (d) Fully-magnetized state.

Three factors determine the magnetic moment of a single free atom: (1) the orbital angular momentum of nucleus, (2) the electron spin, and (3) the orbital momentum change of electrons caused by the external magnetic field. All these three factors can be considered as bound charges.

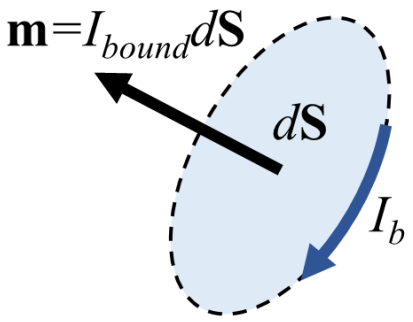

Fig. 3 Schematic of simplified magnetic dipole model for single atom.

To simply the problem, we establish a magnetic dipole moment model for a single atom, as shown in Fig. 3. In this model, I_{bound} represents the bound current induced by the bound charges, circulating the nucleus and forming a small area, $d\mathbf{S}$. The magnetic dipole moment generated by this current can be represented as

$$\mathbf{m} = I_{bound} d\mathbf{S}$$

Depending on the materials properties and the external magnetic field density, the adjacent magnetic dipoles may not be in the same direction. Thus, within a small cubic volume $\triangle$v, the total magnetic dipole moment is given by

$$\mathbf{m}_{\text{sum}} = \sum_{i=1}^{n_{\Delta v}} \mathbf{m}_i$$

Where $\mathbf{m}_i$ is each of the individual magnetic dipole moment, $n_{\triangle v}$ is the number of dipoles that are located within this cubic volume. Subsequently, each $\mathbf{m}_i$ can be considered "identical" under the circumstance where $\triangle$v is infinitely small. Hence, the magnetic dipole density at this point can be quantified as

$$\mathbf{M} = \lim_{\Delta v \to 0} \mathbf{m}_{\text{sum}} = \frac{1}{\Delta v} \sum_{i=1}^{n_{\Delta v}} \mathbf{m}_i$$

Where **M**, also known as the magnetization, is used to describe the magnetic dipole moment per unit volume ($\text{A} \cdot \text{m}^{-1}$).

2.1.2 Magnetic Domain:

Under un-magnetized condition and room temperature, the dipole orientation in the magnetic thin film may have two kinds of "initial state": randomly orientated or locally aligned, as shown in Fig. 2 (a)(b). For both of the cases, the total magnetic field will be

canceled-out to zero. To be more specific, the CoZrTaB, which is categorized into ferromagnetic materials and used as our magnetic thin film, shows the latter behavior. In Fig. 2 (b)(c), one part within which all the dipoles are in the same direction is called a magnetic domain and the boundary between adjacent domains is defined as domain walls. When the magnetization happens, those domains whose dipole direction is the same as the applied field will be the advantageous ones, expanding and annexing the adjacent domains.

2.1.3 Magnetic Flux Density and Permeability

Magnetic flux density (B) reflects total effect on a charged particle (e.g. an electron) that a magnetized material can give, including the magnetization field of the bulk material and the external applied field, written as:

$$\mathbf{B} = \mu_0(\mathbf{M} + \mathbf{H})$$

Where μ_0 is the vacuum permeability. So, it can be simplified as $\mathbf{B} = \mu_0\mathbf{H}$ under vacuum. Also, the coefficient χ_m, magnetic susceptibility, can be inserted to indicate the relation between applied field and magnetization field, which is written as $\mathbf{M} = \chi_m\mathbf{H}$. Then the B-H relation can be further expressed as:

$$\mathbf{B} = \mu_0(\mathbf{H} + \chi_m\mathbf{H}) = \mu_0(1 + \chi_m)\mathbf{H} = \mu_0\mu_r\mathbf{H} = \mu\mathbf{H}$$

Where μ_r is the relative permeability, and μ is the permeability.

Permeability is one of the most important parameters because it, mostly, determines how much a certain material can increase the inductance when it is used as the magnetic thin films in an inductor.

2.1.4 Hysteresis Loop

In order to estimate the performance of a magnetic material, a hysteresis loop (M-H loop) is introduced. In our experiment, this data was taken by an SHB-109 looper, which can generate an AC applied magnetic field ranging from positive to negative value under a certain frequency, and then measures the corresponding magnetization of a sample, displaying the M-H hysteresis curve. Fig. 4 shows an example data taken from a CoZrTaB thin film. In these plots, some important parameters can be extracted.

First, the easy axis and the hard axis are the two directions from which different M-H loops can be measured, and a larger applied field is required for the hard axis to reach the saturation magnetization (M_s). This field is defined as the anisotropy field (H_k), as shown in Fig. 4 (a).

Second, in the zoom-in plot (Fig. 4 (b)), the coercivity (H_c) can be extracted as the field at which the material is demagnetized (M=0), and the remnant magnetization (or remanence, M_r) which is the magnetization value when the applied field is eliminated (H=0). In some cases, the normalized magnetization is used for easier comparison between the two axes (Fig. 4 (c)).[25]

Here the anisotropy properties have been observed in our magnetic thin film, where the different M-H loop can be measured when the applied field direction is changed. For single crystal magnetic thin film (such as single crystal Nickel or Iron), the anisotropy originates from initiative distribution of magnetic domains in each of which the magnetic dipoles are parallel, as described in 2.1. However, for those amorphous structure thin films (such as CoZrTaB that we used), this reason is not enough because the local anisotropy would cancel out completely under the high extend of randomness. The actual case is that the

random local anisotropy does not cancel out completely and, thus, establish the anisotropy properties in amorphous magnetic thin films.[26-28]

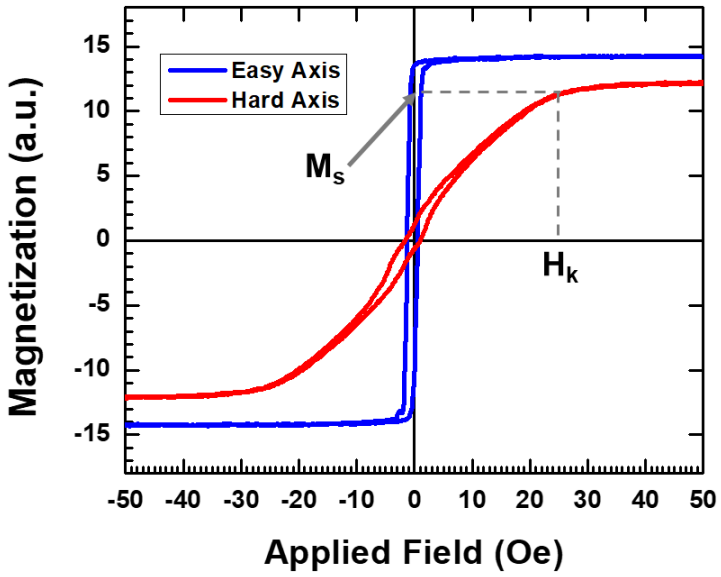

(a)

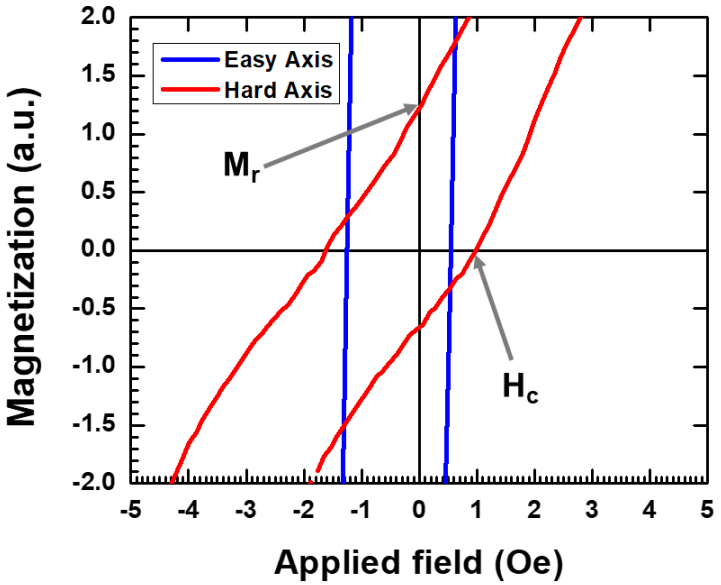

(b)

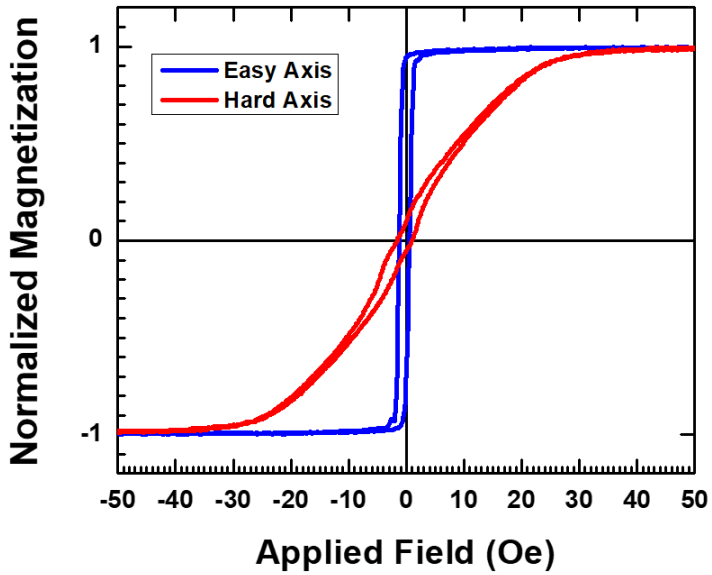

(c)

Fig. 4 Examples of M-H loops. (a) Un-normalized M-H loop with saturation magnetization (M_s) and anisotropy field (H_k) indicated in the plot (b) zoom-in B-H loop with remnant magnetization (M_r) and coercivity (H_c) indicated in the plot (c) Normalized B-H loop.

2.2 Magnetic Thin Film Requirement

In order to achieve a good performance by adding the magnetic core, there are some requirements for the magnetic thin film properties.

First, the permeability value is directly related to the inductance. For example, the inductance of a solenoid inductor with a magnetic core in the center can be expressed as:[29]

$$L = \mu \frac{N^2 \cdot A}{l}$$

Where L is the inductance value, μ is the permeability of the core material, N is the number of turns, A is the inner core area, and l is the length of the inductor coil.

From the B-H equation, we can see that $\mu \propto \left(1 + \frac{M}{H}\right)$. It has to be noticed that permeability from hard/easy axis is different and the magnetic thin film's contribution to increasing inductance varies depending on how we align the hard/easy axis with the Cu trace, as demonstrated in Fig. 5. As a result, the region that can contribute to increasing permeability is the linear part (before saturation) and the hard axis will be more preferable due to extremely small saturation filed of the easy axis for most of the ferromagnetic materials. So, the value of $\mu_0 \left(1 + \frac{M_s}{H_k}\right)$ can be used to estimate the permeability, and high M_s and low H_k will be desired.

Second, to control the core loss, low M_s/M_r and high resistivity are required, and the core loss consists of the hysteresis loss and eddy current loss. In particular, under AC magnetic field, the induced eddy current in the magnetic core results in the power dissipation and the value of it at the length of a cycle can be approximated by:[30]

$$P = \frac{10^{-16} \cdot \pi^2 \cdot d^2 \cdot B_0^2 \cdot f^2}{6\rho} \ W \cdot cm^{-3}$$

Where d is the thickness of magnetic core, B_0 is the flux density amplitude at the surface, f is the frequency of magnetic field, and ρ is the resistivity of magnetic core.

Besides, the hysteresis loss can be measured as the total work in one "zero magnetization-saturation-demagnetization" cycle, which is, in other words, proportional to the area that has been enclosed by the M-H loop, as shown as the shaded portion in Fig. 6. Subsequently, a smaller M_s or M_r will shrink the area, resulting in reducing the loss.

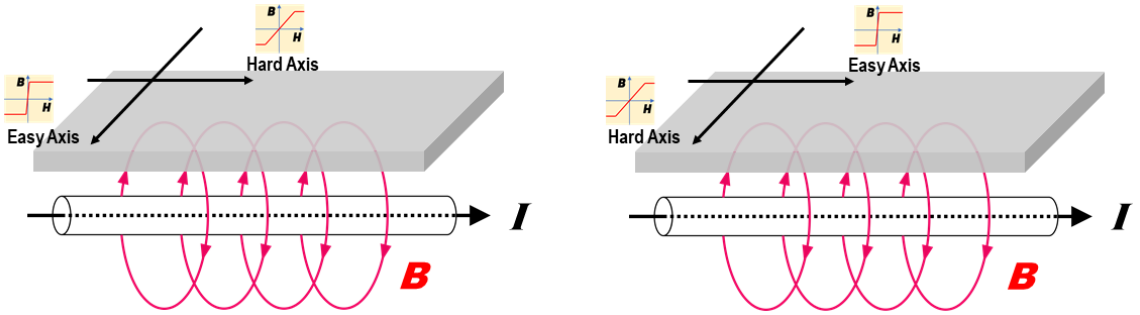

Fig. 5 Schematic of a straight-line Cu trace with magnetic thin film. ***I*** represents the current in the Cu trace and ***B*** represents the induced magnetic field. The direction of induced magnetic field is in parallel with (a) easy axis (b) hard axis of the magnetic thin film.

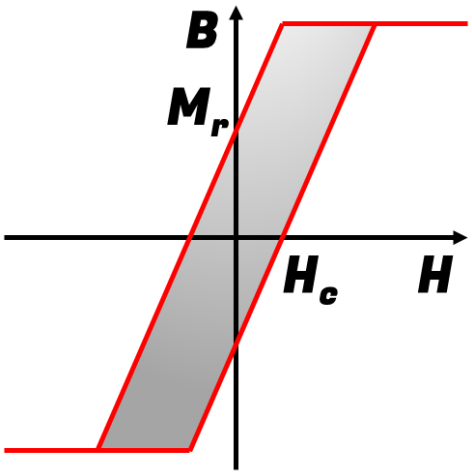

Fig. 6 An example of M-H loop with H_c and M_r highlighted. The shaded portion that has been enclosed by the M-H loop represents the hysteresis loss.

2.3 Characterization of Magnetic Thin Films

2.3.1 Sample Preparation

The magnetic thin film was deposited by the Lesker PVD (DC power source) system at ASU Nanofab with 84Co-4Zr-4Ta-8B (atomic %), 99.5% pure target. The sputter chamber was pumped down to 7.0×10^{-7} Torr to minimize any moisture or contamination. The

power was set to 220W. A low doped high resistivity ($\geq 2000\ \Omega \cdot cm$) 3-inch Silicon wafer was used as the default substrate if not specified in the paper.

For the lamination structure, two methods were used to create the insulator layer in between: (1) Oxidation method. The chamber gas flow was switched to pure oxygen for 10 minutes and the DC power was turned off after each of the individual lamination layer (CoZrTaB) was finished. An oxide layer was formed at the expense of the surface of as-deposited CoZrTaB under this oxygen ambient. The next layer would be deposited on this oxide layer. (2) Extra deposited SiO_2 layer. A 10 nm SiO_2 layer was deposited on each individual lamination layer with RF power and SiO_2 (amorphous) target. The sputter system has multiple guns, which allows us to install two different targets and the vacuum does not need to be compromised.

2.3.2 Sputter Pressure Optimization

For most of the PVD system, the working pressure is an important parameter because it can affect the atomic disorder, which is strong related to most of the magnetic properties, such as H_c, H_k, M_s and resistivity. Some early research[31, 32] on CoZrTaB thin film shows that an amorphous structure can give a high permeability, and a ultra-high sputter power and high pressure were used to achieve the more “amorphous” thin film. However, the latest investigation[33] indicates that too high of a sputter pressure might cause a perpendicular magnetic anisotropy (PMA), which is the main reason that the in-plane magnetic properties are sacrificed. So, there could be a sputter pressure trade-off between amorphous structure and the appearance of PMA, so that the best value for each PVD system may vary.

In the three individual sputter sessions, we used the 3 mTorr, 6 mTorr, and 9 mTorr to deposit the 400 nm CoZrTaB without any applied magnetic field. The related parameters are shown in Table 2. The RMS of the root mean square (RMS) of the as-deposited surface was measured by Bruker Multimode 8 AFM instrument. The surface roughness is dependent upon the pressure, but the rate versus pressure is not linear and the 6 mTorr sputter results in the lowest rate and roughness. This result is consistent with the scanning electron microscopy (SEM) pictures taken by the Hitachi S-4700 Field Emission Scanning Electron Microscope shown in Fig. 7. Only in 3 mTorr sample SEM picture can we see the fully distributed vertically columnar structure; by contrast, the partially dark area can be seen in 6/9 mTorr samples. According to the latest research,[33] the appearance of this structure can diminish the in-plane magnetic properties, especially for the M_s and H_c. Fig. 8 shows the atomic force microscopy (AFM) images captured on a $1.5\ \mu m \times 1.5\ \mu m$ surface of each sample, indicating that the grain size of 6/9 mTorr samples is larger due to a higher disorder level. The additional X-ray diffraction characterization (XRD) results (shown in Fig. 9) indicate the absence of Co-related peaks and amorphous structure in the magnetic thin films.

Table 2
Comparison of Deposition Rate and Surface Roughness (RMS) of Different Sputter Pressure

Sputter pressure (mTorr)	3	6	9
Deposition rate (A/s)	2.48	1.81	2.01
RMS (nm)	2.34	1.86	1.92

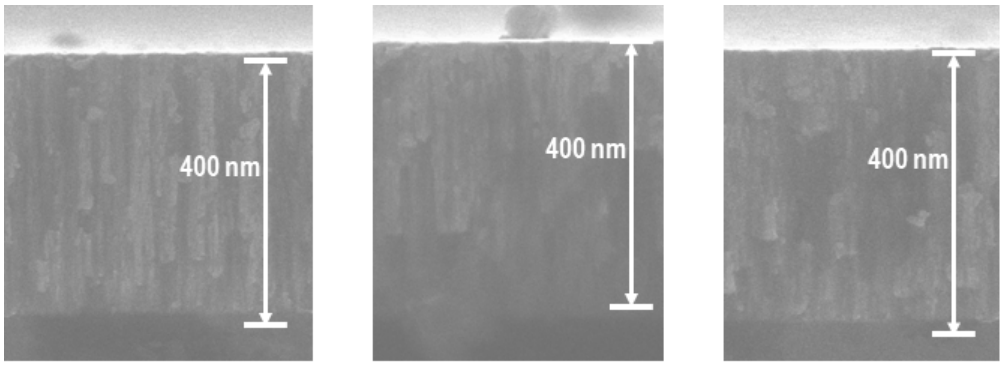

(a) (b) (c)

Fig. 7 Cross-sectional SEM images of 400 nm CoZrTaB thin film on Si substrate. The sputter pressure is (a) 3 mTorr (b) 6 mTorr (c) 9 mTorr.

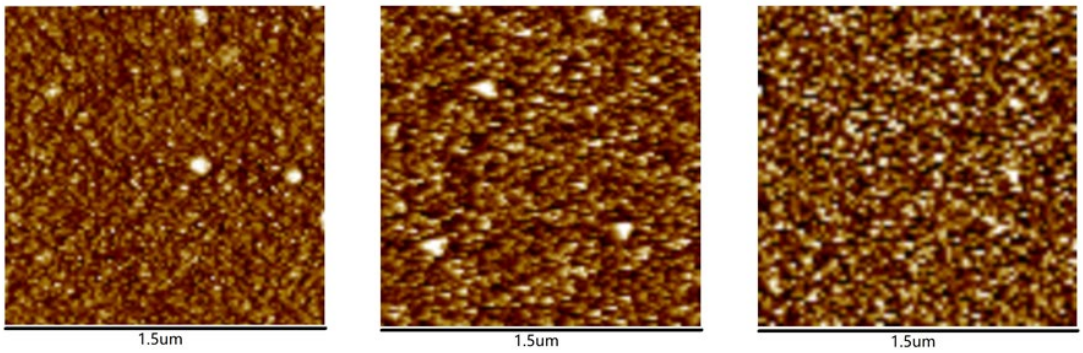

(a) (b) (c)

Fig. 8 AFM images of the 400 nm CoZrTaB thin films deposited under (a) 3 mTorr (b) 6 mTorr (c) 9 mTorr.

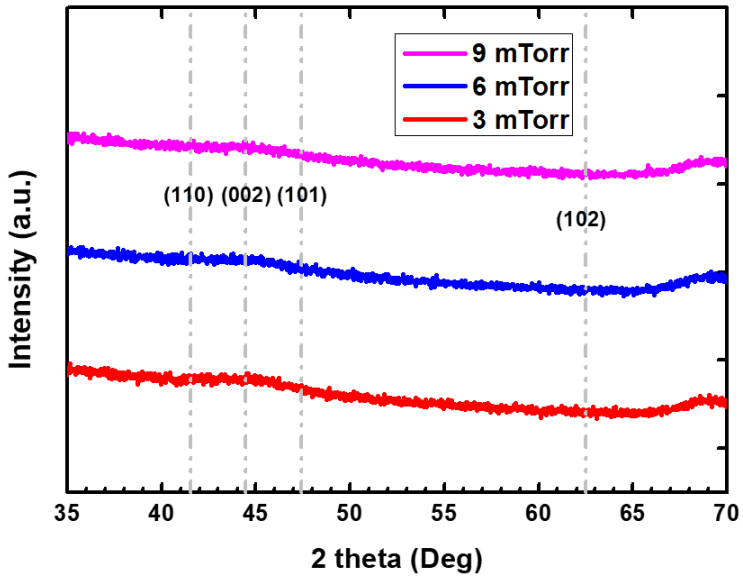

Fig. 9 The XRD result of 400 nm CoZrTaB thin films on Si sputtered under different pressures. $2\theta = 21.55°, 44.47°, 47.41°$ and $62.52°$ have been marked as the grey dotted lines and represent (110), (002), (101), and (102) planes of the crystalline Cobalt. The absence of these peaks proves amorphous structure in the thin films.

The M-H loops and parameters of 400 nm CoZrTaB thin film under three sputter pressures are shown in Fig. 10 and Table 3. From definition, we know that magnetic anisotropy exists in all ferromagnetic materials; and biaxial anisotropy is very often seen, in which the easy axis is parallel to the easiest orientation to magnetize the material, compared with the hard axis parallel to the hardest magnetization orientation.[34] Here, each sample is observed to have hard/easy axis, which are observed to be perpendicular to each other.

The comparison of the normalized M-H loop also proves the above measurement results. In Fig. 10(a), the 3 mTorr sample has a much higher H_c (22.8/23.5 Oe for easy/hard axis) than other two samples (8.8-10.9 Oe). Considering the H_k, the 3 mTorr sample does not saturate when the applied field is 75 Oe (This is the maximum scan range of the current coil setup of SHB looper).

For the other two samples, though the easy axes of them behave similarly, the hard axes vary: in the low applied field region (< 20 Oe), the 6 mTorr sample has almost the same loop track compared with its own easy axis, while the M-H slope of 9 mTorr sample slightly deteriorates; in the high applied field region (20 ~ 50 Oe), both of the sample saturate under 50 Oe applied field. Overall, the 6 mTorr sample has the lowest H_k, suggesting its hard axis can provide the highest permeability, though the H_c of it is slightly worse. So, 6 mTorr will be used as the default sputter pressure in the following discussion if not specified.

To deeply understand the mechanism, the coercivity H_c can be written in an empirical equation:[35]

$$H_c = \alpha \frac{2K_1}{M_s} - N_{eff} M_s$$

Where α refers to the structure reduction factor and is determined by temperature and the microstructure of the material, K_1 is the first order anisotropy constant, M_s is spontaneous magnetization, and N_{eff} is average local effective demagnetization factor. The dependency of temperature is ignored because our experiment is performed under room temperature. So, only the microstructural correlation will be considered. Here a higher disorder level induced by the increasing sputter pressure results in stronger (or larger number of pinning sites in the thin film, which can elevate the N_{eff}. However, the change in the pinning sites if the sputter pressure is too high could result in a worse M-H slope and multi-domain slope would appear (seen in the 9 mTorr M-H loop).

In addition, the M_s has not been discussed because the SHB looper has not been calibrated. However, all of the three samples have been observed to have a higher M_s on easy axis, compared the one on their own hard axis.

Table 3
Main Parameters of 400 nm CoZrTaB Thin Film on Si Substrate under Three Sputter Pressure

Sputter pressure	3 mTorr		6 mTorr		9 mTorr	
Axis	Hard	Easy	Hard	Easy	Hard	Easy
Squareness (M_r/M_s)	≤ 0.72	≤ 0.70	0.49	0.68	0.44	0.70
H_c (Oe)	23.5	22.8	10.2	10.9	9.7	8.8

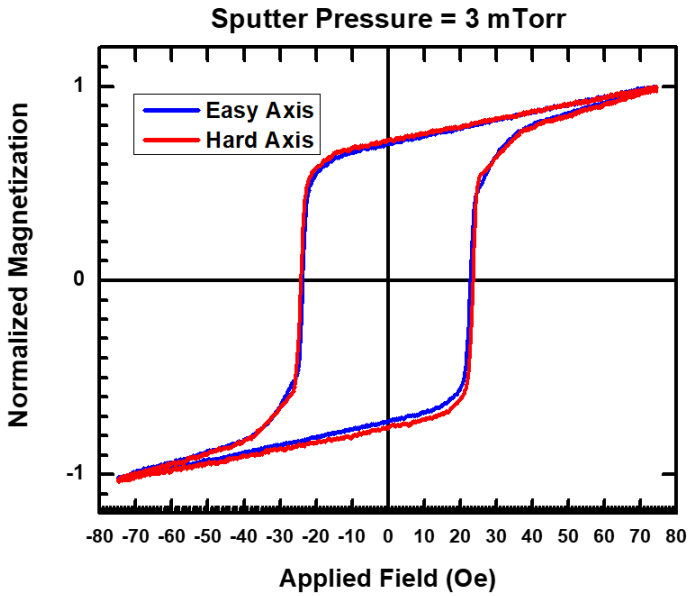

(a)

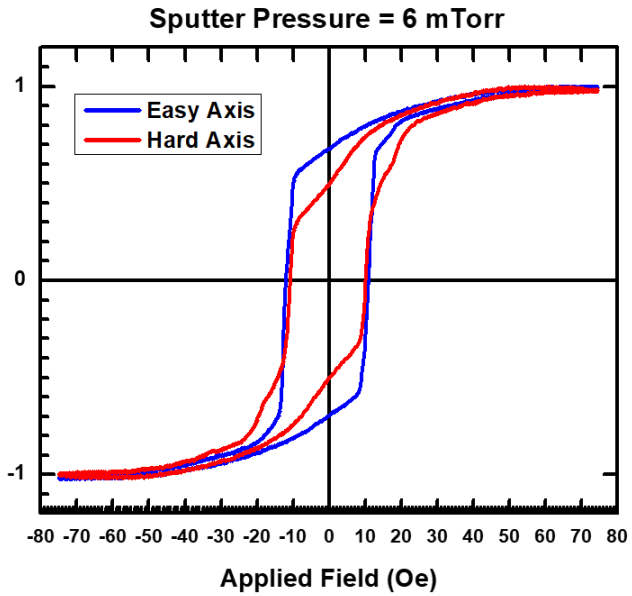

(b)

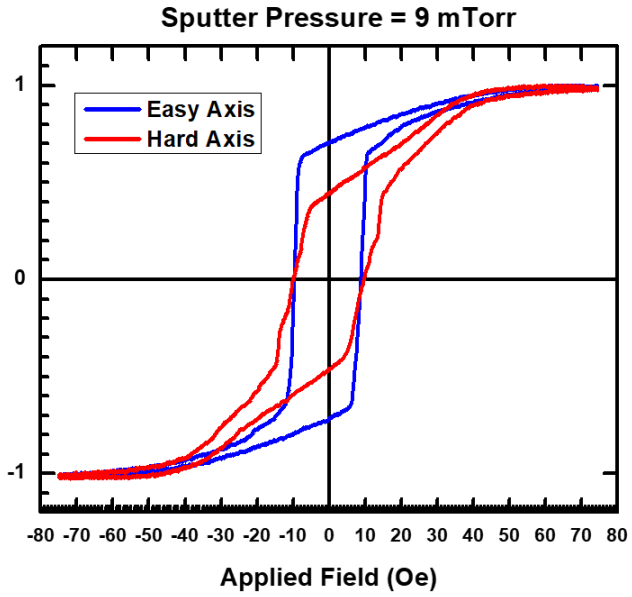

(c)

Fig. 10 M-H loop of 400 nm CoZrTaB thin film on Si substrate with sputter pressure of (a) 3 mTorr (b) 6 mTorr and (c) 9 mTorr.

2.3.3 Lamination Structure Optimization

There are several specifications that can determine the performance enhancement of introduction of lamination structure into CoZrTaB magnetic thin film, including number of layers, layer thickness, and insulator layer details. In this paragraph, we mainly focus on the insulator layer effect. The former two factors will be discussed in the next chapter.

As described in Chapter 2.3.1, the two methods can create the insulator layer between each two lamination layers, which can reduce the eddy current induced in the magnetic thin film and, thus, decrease the core loss.

Basically, the lamination structure investigated here is based on the stacking of individual 100 nm CoZrTaB thin film. Fig. 11(a) shows the M-H loop of a single layer thin film as the baseline performance. The H_c is 2.9 Oe for both axes, and the saturation field is 27.1 Oe and 49.3 Oe for easy/hard axis, respectively.

The M-H loop comparison of the 4×100 nm laminated CoZrTaB thin film is shown in Fig. 11. The multi-domain phenomenon is severe in Fig. 11(b), in both of the easy axis and hard axis, and the transition point is at 7 Oe and 16 Oe, at which the slope of loop begins to change. Due to the relation between the slope and permeability, the appearance of this phenomenon will deteriorate the inductance when the drive current goes higher, which will induce a larger magnetic field, thus, the permeability could decrease if the field is beyond the transition point. This phenomenon, which always emerges with enlarging H_c, can be explained by the movement of domain walls (pinning, interactions, nucleation and annihilation), which can be tuned by changing deposition recipe or the substrate roughness/stress.[36, 37]

On the other hand, the lamination thin film with SiO_2 insulator (Fig. 11 (c)) demonstrates a much more ideal behavior for the easy and hard axis, suggesting it can provide a stable permeability under the whole applied field range (±30 Oe). Besides, in the comparison of H_c, the SiO_2 sample also shows advantage, which can be explained by the magnetostatic interaction between layers.[35, 38] The detailed comparison is listed in Table 4.

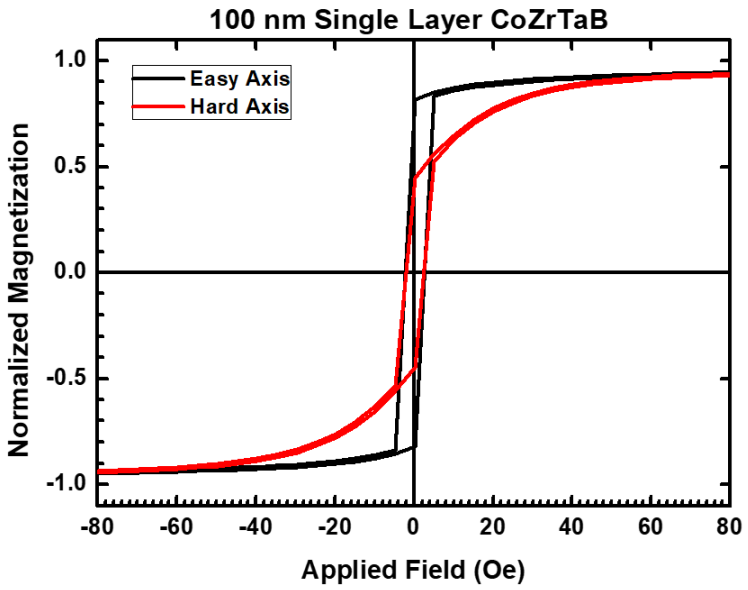

(a)

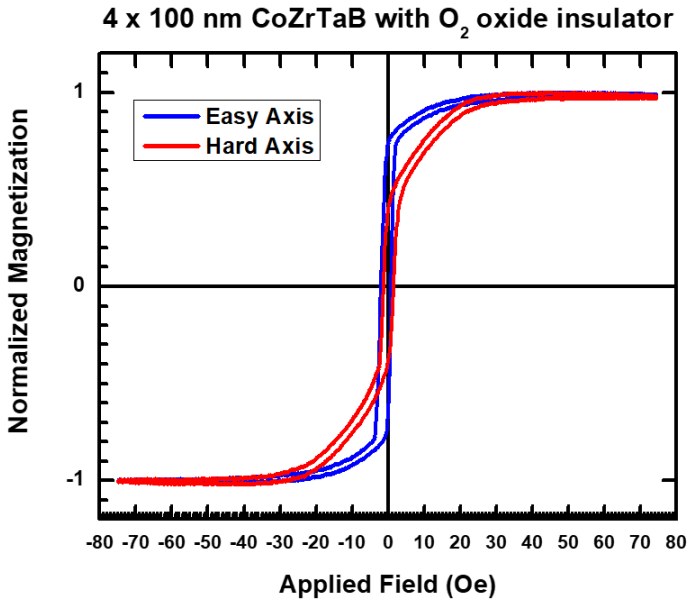

(b)

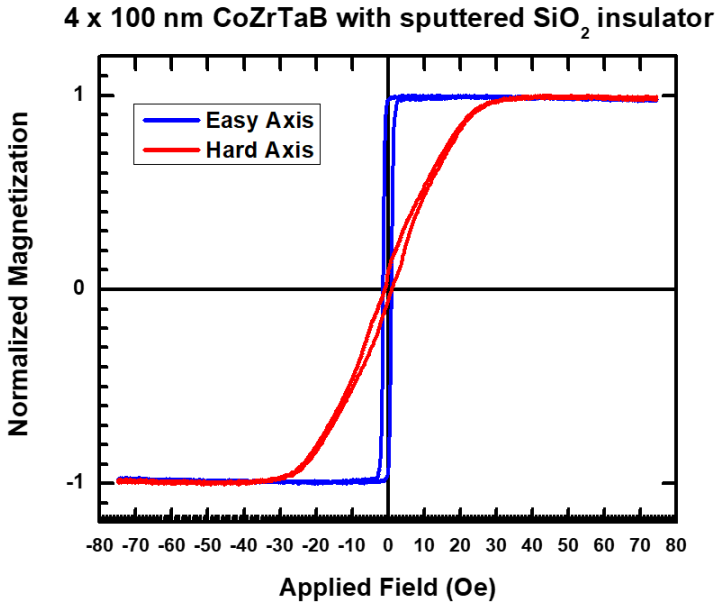

(c)

Fig. 11 M-H loop of (a) 100 nm CoZrTaB thin film on Si, and 4×100 nm laminated CoZrTaB thin film on Si with (b) O_2 oxidation insulator layer and (c) sputtered SiO_2 insulator layer.

Table 4
Main Parameters of 4×100 nm CoZrTaB Thin Film on Si Substrate with Two Kinds of Insulator Layer

Insulator type	O_2 oxide layer	Sputter SiO_2 layer
Easy axis coercivity H_{c_e} (Oe)	1.5	1.2
Easy axis saturation field (Oe)	11.3	0.7
Hard axis coercivity H_{c_h} (Oe)	1.6	0.9
Hard axis saturation field (H_k) (Oe)	19.7	22.9
Squareness (easy/hard axis)	0.74/0.39	0.98/0.09

Fig. 12 show the cross-sectional SEM images of 4×100 nm laminated CoZrTaB thin film with two kinds of insulators. We can see that some grains can grow across the oxide layer if we use the oxidation method and this can explain some negative performance in the M-H loop measurement: the imperfection of lower lamination layer can accumulate and be remained when the next higher layer deposition starts. However, these "defects" can be suppressed or eliminated when an extra SiO_2 layer is sputtered in between, even if it is only 10 nm.

Also, many early researches[39-41] show that the insulator in the lamination structure, acting as the substrate of the above layer, can greatly change the hysteresis loop and could be used as a method to optimize the magnetic properties due to their widely different mechanical properties (such as stress or tensile). This can explain the fact that 4×100 nm CoZrTaB with SiO_2 even has better magnetic properties than a single 100 nm layer.

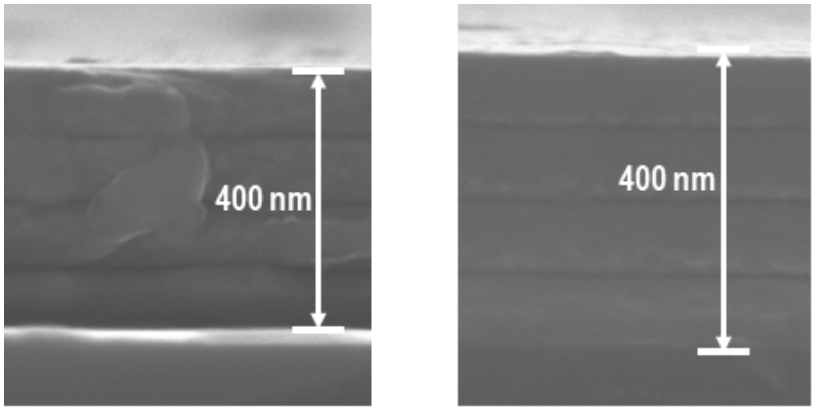

(a) (b)

Fig. 12 Cross-sectional SEM images of 4×100 nm CoZrTaB thin films on Si substrate with (a) O_2 oxidation insulator layer and (b) sputtered SiO_2 insulator layer.

2.4 Magnetic Thin Films on Organic Substrates

The previous paragraphs discuss the CoZrTaB thin films on Si substrate, but this is not fully compatible with the device application scenario, which requires those passive components to be integrated on or into the organic packaging materials. The performance degradation are often seen in the magnetic thin film deposition on the non-Si substrate.[7, 21] Several factors determine the degradation level, such as the surface roughness, deformation during the thermal process, interface mismatch. Here we will discuss the optimization of CoZrTaB thin film on 2 kinds of polyimide substrates.

In the polyimide substrate preparation steps, two kinds of precursors (PI-2555 and HD-8820) were coated on the 3-inch Si wafer with spinner at 3000 rpm for 30 seconds, followed by the 280℃ curing for 60 minutes.

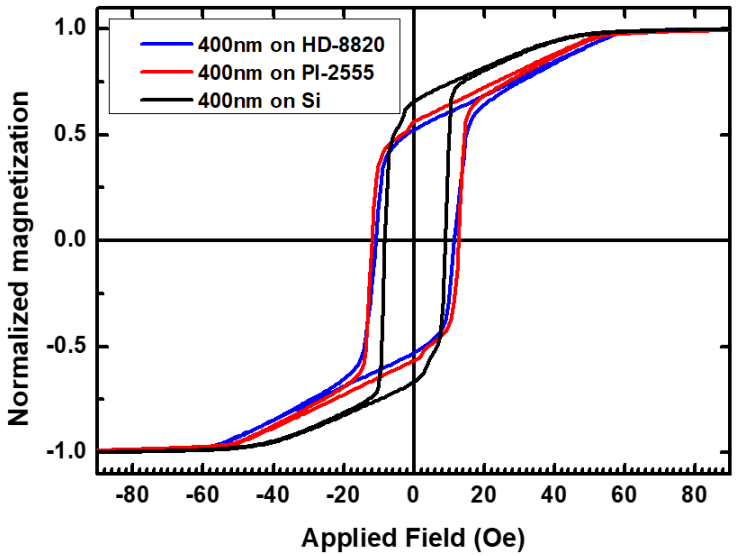

Fig. 13 M-H loop of 400 nm CoZrTaB thin film on Si and two polyimide substrates.

The comparison of 400 nm CoZrTaB on these substrates is shown in Fig. 13. The degradation happens in both H_k and H_c. The added tensile or stress force in the surface and the much greater deformation coefficient compared to Si can explain this, since the heat generated during the deposition process could cause the deformation of polyimide layer, further increasing the interface "mismatch". Empirically, the substrates will be heated to 50-80 ℃ after depositing 400 nm thin film in our PVD system, and the thermal expansion coefficient is 40 and 67 ppm, respectively, for cured PI-2555 and HD-8820. The additional test on the same substrates cured under 380℃ shows slightly improved H_k and H_c, but this extremely high temperature is likely to be incompatible with other fabrication process. So, 280℃ will still be used as the curing temperature in the following steps.

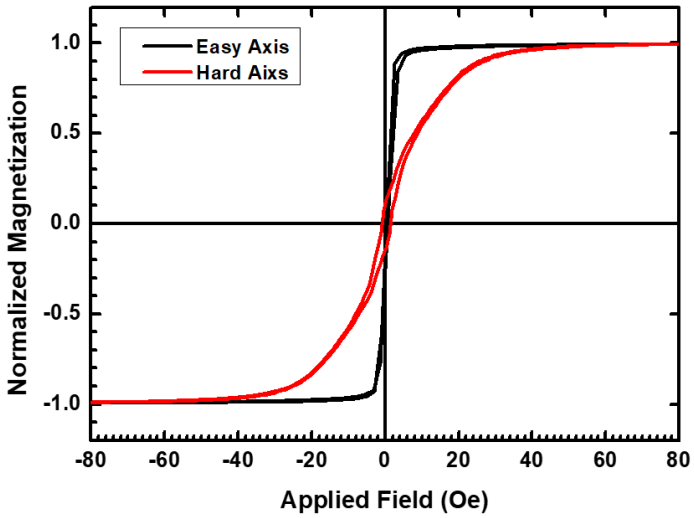

(a)

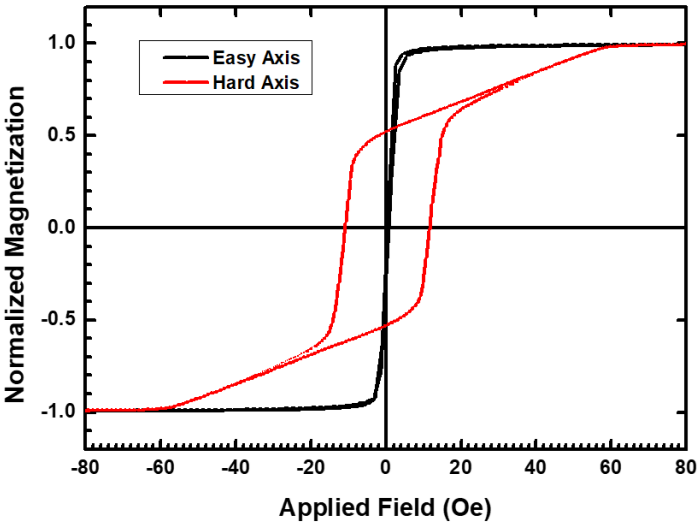

(b)

Fig. 14 M-H loop of 4×100 nm CoZrTaB thin film on (a) PI-2555 substrate and (b) HD-8820 substrate.

Table 5
Main Parameters of 4×100 nm CoZrTaB Thin Film on Two Polyimide Substrates

Substrate type	PI-2555	HD-8820
Easy axis coercivity H_{c_e} (Oe)	1.4	<1
Easy axis saturation field (Oe)	5.3	4.6
Hard axis coercivity H_{c_h} (Oe)	1.4	15.3
Hard axis saturation field (H_k) (Oe)	26.2	47.3
Squareness (easy/hard axis)	0.1/0.1	0.1/0.5

Then, the comparison of two substrates for the 4×100 nm laminated CoZrTaB thin films is demonstrated in Fig. 14. Sputtered SiO_2 was used as insulator in these samples. Basically, the degradation on PI-2555 sample is acceptable, while the HD-8820 sample has a much higher H_c and the appearance of multi-domain in the hard axis dramatically deteriorates H_k. The details of two samples are listed in Table 5.

Consequently, in the following fabrication process, the PI-2555 polyimide will be used as substrate and the lamination structure will be utilized in the CoZrTaB thin film for a better integration performance.

2.5 Conclusion

In this chapter, a comprehensive optimization on CoZrTaB thin film is conducted, including the deposition recipe, lamination profile, and its M-H loop change on different polyimide substrates. We can see that the laminated CoZrTaB with SiO2 insulator can achieve high H_k (26.2 Oe), low H_c (1.4 Oe), which is more aligned with our application

requirement. This is fundamental to the next step of device simulation and optimization because the M-H loop data can be imported.

CHAPTER 3

INDUCTOR DESIGN AND OPTIMIZATION

3.1 Simulation Software

We used Ansys Maxwell to design, simulate and optimize the device. Compare with Ansys HFSS, this software provides an option to import the M-H loop of the magnetic material instead of using a static permeability value. This feature can assist us improve the simulation by implementing a more "real" properties of the magnetic thin film, which aligns with our M-H loop measurement data. Fig. 15 show the M-H loop that has been imported and the parameters are listed Table 5, PI-2555 sample. The B_{sat} value is 1.3 Tesla from our group's previous measurement, and the conductivity is 869570 Siemens/m.

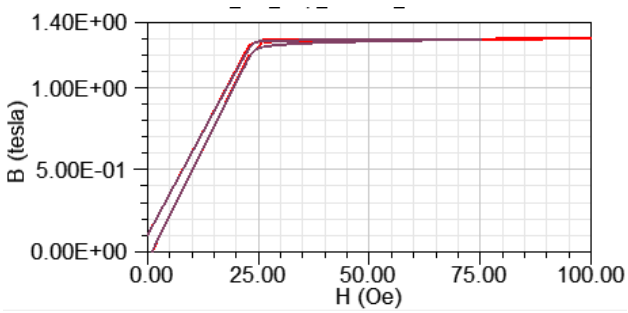

Fig. 15 The M-H loop that has been imported into the Maxwell simulation.

3.2 Copper Trace Design

In this research, single-turn Cu trace is used as the air core inductor, as shown in Fig. 16. Compared with other complicated inductor topology (spiral, solenoid, and toroidal), the single-turn pattern has the advantage of low DC/AC resistance and fabrication complexity (which does not require Cu via). Based on the material selection in the fabrication step, the thickness and width of Cu trace is set to be 18 μm and 130 μm. The size limit is 1.5 mm^2

based on the specification requirement of the application scenario of this project. Here we mainly discuss the optimization of L_1 and L_2. Four prototypes were created in the simulation software with the dimensions shown in Table 6, and the related parameters (inductance, AC resistance, and quality factor) were extracted, shown in Fig. 17. The quality factor can be expressed as:

$$\mathrm{Q} = 2\pi f \frac{\mathrm{L}}{\mathrm{R}}$$

Where f is the frequency, L is the inductance, R is the AC resistance.

The DC resistance can be approximated by

$$DCR = \rho \frac{l}{S}$$

Where $\rho = 1.68 \times 10^{-8}\ \Omega \cdot \mathrm{m}$ is the resistivity of Cu, l is the total length of trace, and S is cross-sectional area.

Table 6
Dimensions and Calculated DC Resistance of Four Prototypes of Air Core Inductor

Design #	1	2	3	4
L1 (μm)	300	430	600	1116
L2 (μm)	3460	3460	2113	1413
DCR (calculated, $m\Omega$)	54	56	39	36

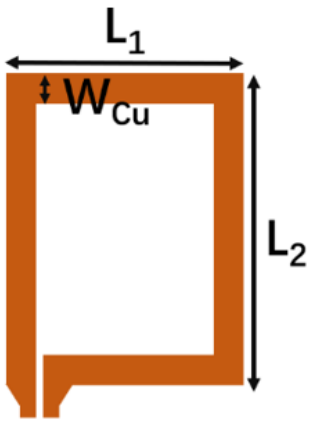

Fig. 16 Schematic of a Copper trace (top view). Some important dimensions are listed, such as side lengths of the rectangle: L_1, L_2, and the width of trace: W_{Cu}.

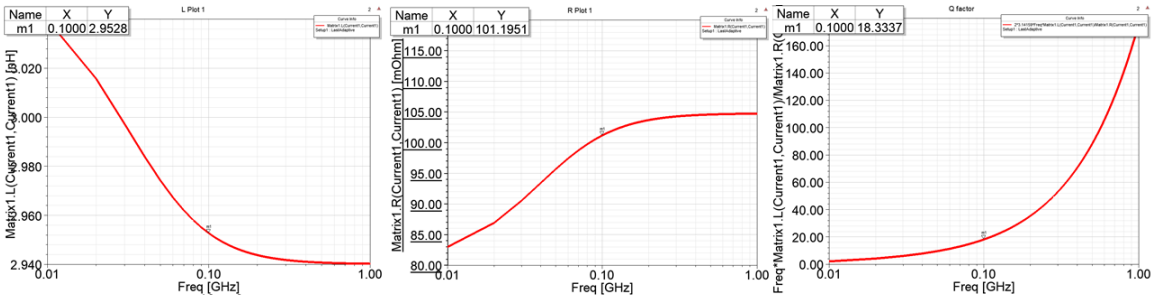

(a)

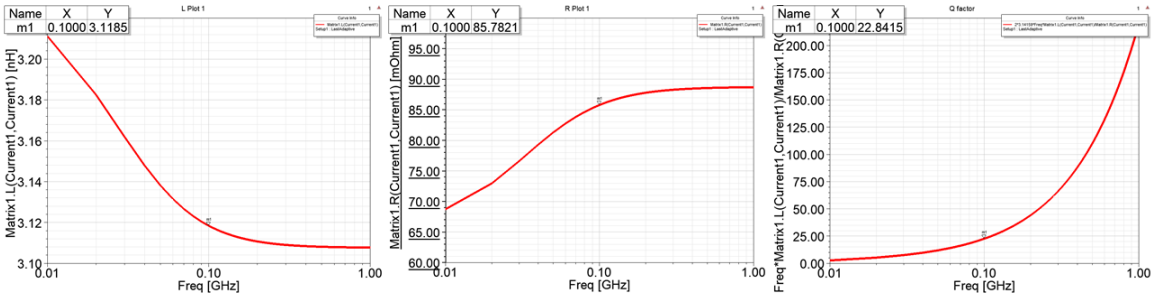

(b)

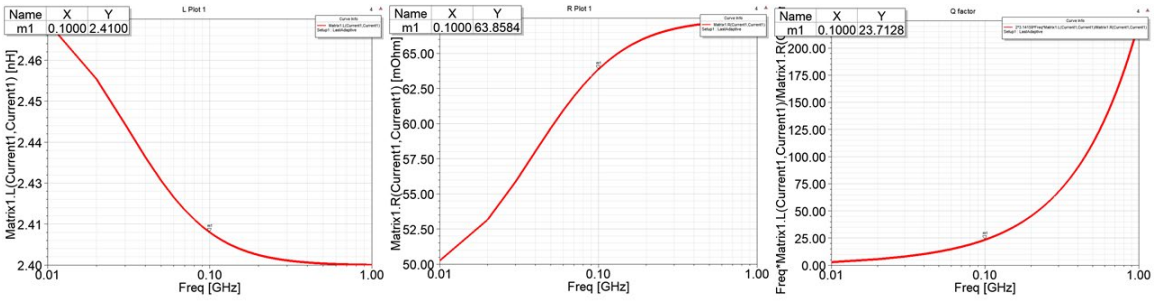

(c)

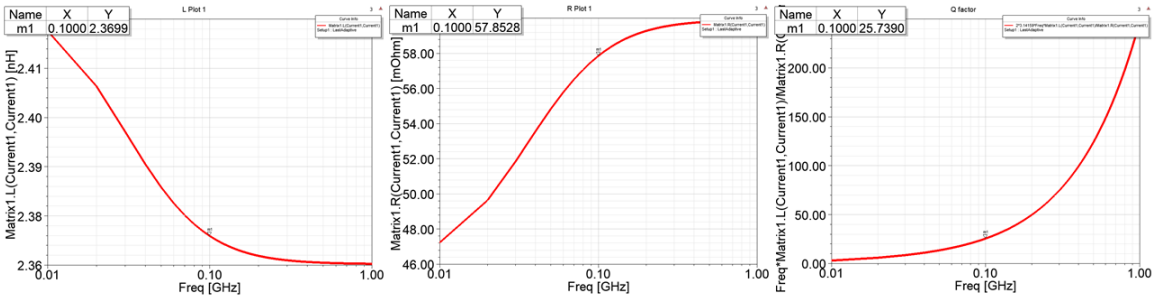

(d)

Fig. 17 Simulation result of inductance, AC resistance, and quality factor for the air core inductor (a) design 1 (b) design 2 (c) design 3 (d) design 4. The frequency range is 0.01 GHz – 1 GHz.

A trend of "being fatter" can be seen from design 1 to design 4. From the simulation results, we can see that design 1 and 2 have higher inductance and ACR, which is in contradiction to design 3 and 4. For this one-turn air core inductor, the interaction between two parallel traces is stronger when their position is getting closer, which can beneficial to the inductance, but also make the ACR worse.

3.3 Magnetic Core Inductor Design

3.3.1 Lamination Structure Optimization

In order to maximize the inductance, a thicker magnetic thin film is desired, and 3 μm is the maximum deposition thickness for our Lesker PVD system. So, the relation between the layer number of lamination and performance needs to be investigated. Here a sandwich-structure magnetic core inductor based on the design 1 Cu trace was created in the simulation software. The total magnetic thickness is 3 μm, with an extra 10 nm SiO_2 spacer between each two adjacent lamination layers. Fig. 18 shows the cross-section schematic of a 5-layer lamination. The size of core is $3200\ \mu m \times 500 \mu m$ and it is located in the center of Cu trace. The gap between core and Cu is $15\ \mu m$. Fig. 19 shows the simulation result at 100 MHz.

We can see that a thicker layer has higher inductance and there is a big inductance-drop when each layer is thinner than 200 nm. We should notice that the total thickness of SiO_2 spacer is 290 nm when the layer number is 30, which is almost 10% of the thickness of the magnetic core. This increasing thickness of SiO_2 will enlarge the distance between the Cu trace and the magnetic core, hence, decrease the magnetization in those lamination layers which are far from the Cu trace.

On the other hand, the eddy current suppression is more obvious when the layer number is larger than 5. In addition, the ACR is less than 0.3 Ω when the layer number is larger than 15. The ACR increased approximately linearly with 1/N (N is the layer number), which can give us a good estimate when the layer number is larger than 30. The simulation time exceeds one day when the lamination thickness is smaller than 150 nm (corresponding N=20). Considering the trade-off between inductance and ACR, we choose 15×200 nm as the lamination profile for the device fabrication step. Compared with the non-laminated

structure, this 15-layer CoZrTaB thin film can decrease the ACR by 47% at 100 MHz and control the inductance loss within 10%.

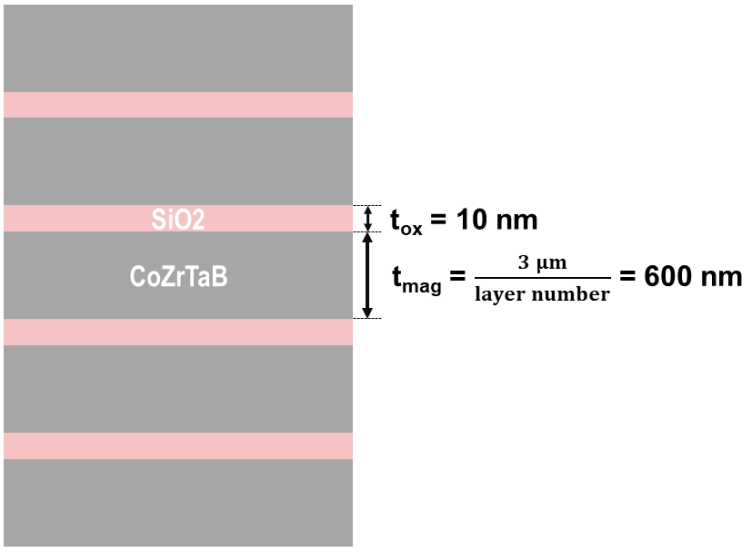

Fig. 18 Schematic of a 5-layer lamination structure of CoZrTaB (in grey), with the 10 nm SiO_2 insulator. The total magnetic thickness is 3 μm.

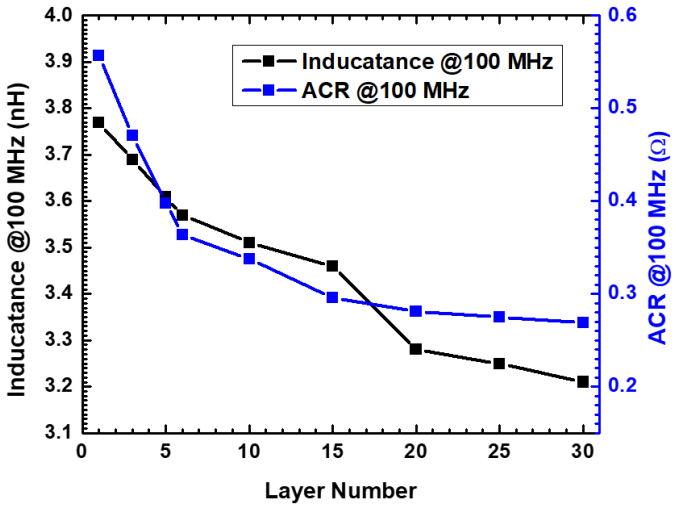

Fig. 19 Inductance and AC resistance with respect to the layer number of lamination structure. The data was extracted by Ansys Maxwell at 100 MHz frequency and the total thickness of the magnetic thin film is 3 μm (the SiO_2 thickness is excluded).

3.3.2 Magnetic Core Pattern Optimization

It is also necessary to optimize the magnetic core pattern to achieve the best performance. Here two types of magnetic core pattern will be considered for each of the Cu trace design, as shown in Fig. 20. Core pattern 1 will cover the whole Cu pattern without any breaks in the center which is expected to provide the highest inductance, of which the two side lengths are defined as $a_1 = L_1 + 200\mu m$, $a_2 = L_2 - 260\mu m$. Core pattern 2 has the same one side length a_2, but there is a blank area in the center, which is a widely-used method to decrease the ACR; the other side length is defined as $a_3 = W_{Cu} + 200\mu m = 330\mu m$. So, the device size will be the same with these two core patterns.

Table 7 shows the simulation results at 100 MHz. Design 2-Core pattern 1 has the highest inductance (3.67nH), but the worst quality factor was achieved due to the ACR deterioration. The best quality factor was obtained with Design 4-Core pattern 2. It is the only design providing quality factor that exceeds 10. Basically, Core pattern 2 has relatively lower inductance, but has advantage in ACR and quality factor. The added magnetic core area can increase the effective volume that could be magnetized, however, increase the eddy current as well. Same trend applies to the Cu pattern design: the thinner the Cu trace is, the higher inductance, but it may suffer from higher energy loss. Trade-off should be considered depending on the application requirement.

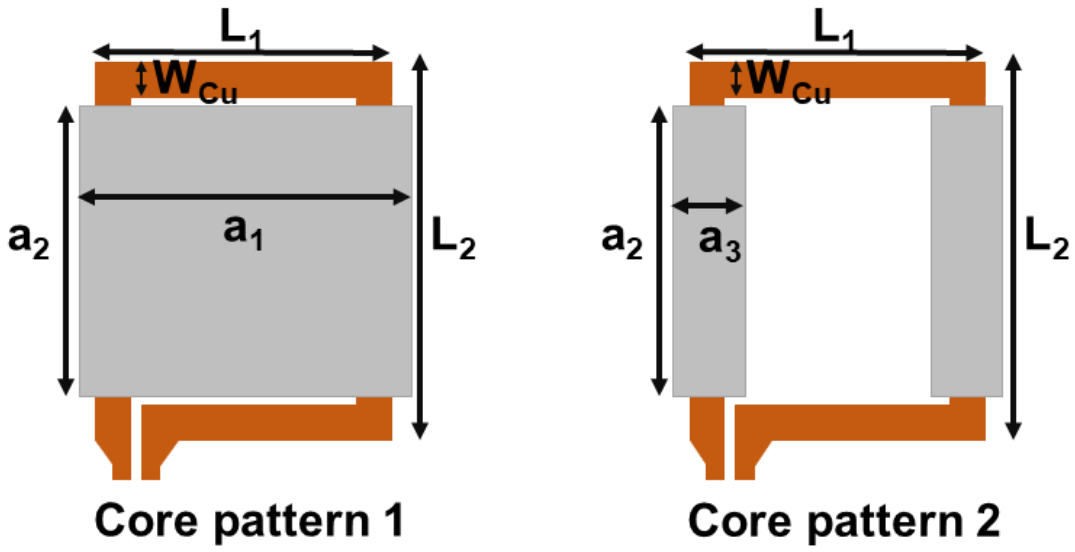

(a) (b)

Fig. 20 Schematic (top view) of (a) Core pattern 1 and (b) Core pattern 2.

Table 7
Simulation Results of Four Types of Cu Pattern and Two Types of Magnetic Core Pattern at 100 MHz Frequency

Design #	1		2		3		4	
Core pattern #	1	2	1	2	1	2	1	2
Inductance (nH)	3.46	3.27	3.67	3.45	3.31	3.22	3.19	3.12
ACR (Ω)	0.296	0.243	0.339	0.303	0.231	0.214	0.203	0.189
Quality factor	7.34	8.46	6.8	7.15	9.00	9.45	9.87	10.37

3.4 Conclusion

The simulation results show that many trade-offs need to be considered on the design. For the air core inductor part, design 2 can be a good candidate because of its balance between inductance and ACR. Design 3 and 4 will be more suitable for efficiency-sensitive

application. When we come to the magnetic core inductor part, the similar trend can be seen: although the obvious inductance enhancement can be seen, the low baseline inductance limits the performance of design 3 and 4 with magnetic core.

Also, the implantation of measured M-H loop into the simulation can improve the accuracy when we modify the lamination structure. Potentially, the accuracy could be further improved by precisely importing M-H loop of each exact lamination structure, which, however, would consume a large amount of sputter targets.

CHAPTER 4

MAGNETIC CORE INDUCTOR FABRICATION

We introduce an innovative fabrication method with utilization of the flipchip bonder to make the sandwich structure magnetic core inductor. The whole process flow is shown in Fig. 21, which starts from two substrates at the same time.

Substrate 1 is initially prepared by a flexible PCB attached to a holding wafer, then the Cu trace pattern is made and covered by polyimide. After this, the magnetic core layer is deposited on the polyimide surface and its pattern is made by lift-off process. The original holding wafer should be removed and a new holding wafer attached to the top surface. Substrate 1 is now ready for the bonding process.

Substrate 2 is initially prepared with a polyimide layer on the holding wafer, on which the magnetic core layer is made on the same deposition and lift-off process when we prepared substrate 1. Then an adhesion material is coated on surface of substrate 2.

The last step is the bonding process finished by the flipchip bonder. In this step, two substrates are aligned and bonded. An extra lithography and dry etch process is needed on the top polyimide layer to expose the Cu trace contact pad for DC/RF measurement.

Process details and material selection will be described in the following paragraph.

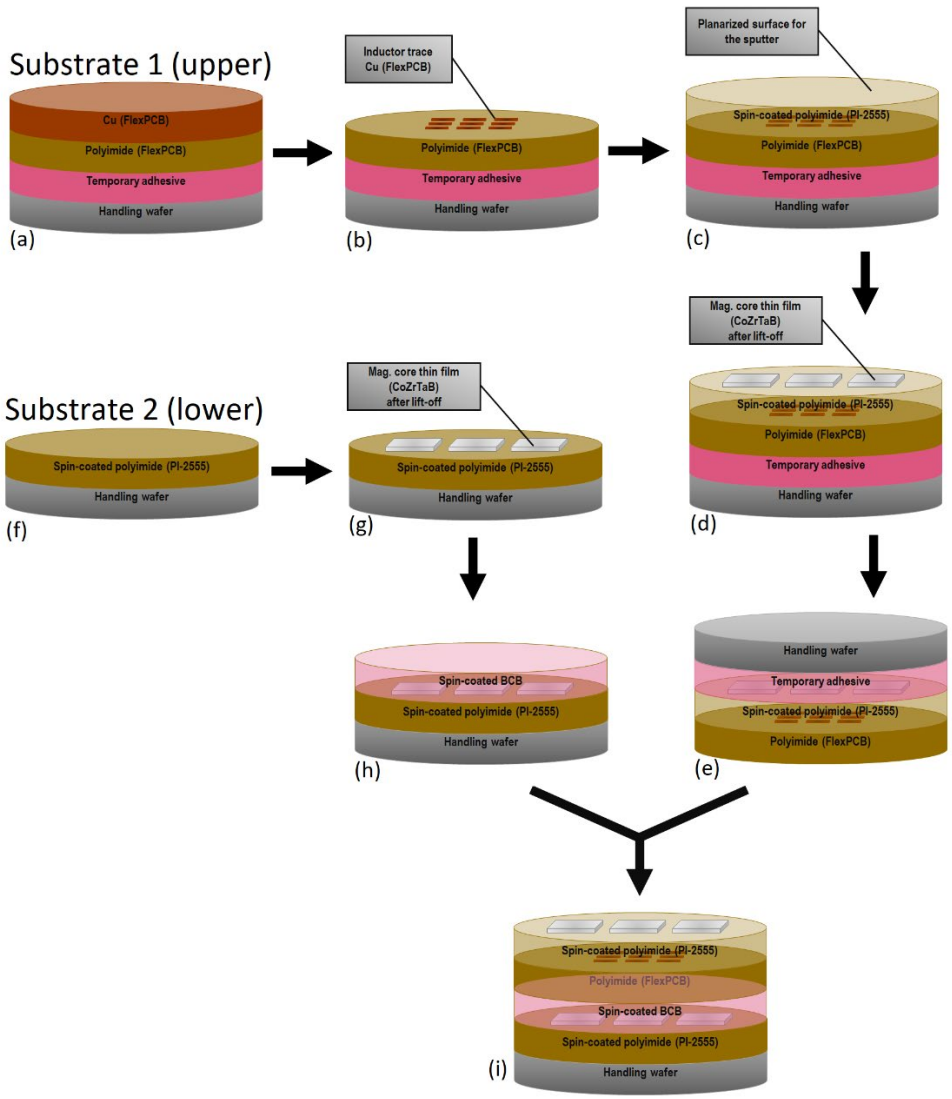

Fig. 21 Fabrication flow chart. The upper layer fabrication process: (a) Flexible PCB attached on a handling wafer. (b) Cu trace pattern finished with wet etch. (c) A planarized polyimide layer added on the Cu trace. (d) Magnetic core patterned by lift-off. (e) Another handling wafer attached to this layer. The lower layer fabrication process: (f) Polyimide on handling wafer. (g) Patterned magnetic core on polyimide. (h) Coating BCB on the magnetic core layer. (i) Finished device after bonding.

4.1 Cu Pattern Preparation

The flexible PCB Cu sheet is purchased from PCBWay and is used as the Cu trace layer.

This material consists of 18μm thick Cu and 25μm thick cured polyimide and it is widely

used for the flexible or wearable device fabrication[42], or as the substrates of MEMS sensor[43].

After the flexible PCB is attached to the handling wafer, the pattern of Cu trace is made with wet etch process, as shown in Fig. 22(a). First, the AZ4330 photoresist is spin coated on the Cu surface and the lithography is finished with OAI 808 aligner; then the flexible PCB with photoresist is immersed into the CE-100 Cu etchants for 10 minutes till the inductor trace patterns can be observed clearly. Over-etch should be avoided by controlling the etch time, especially for the contact pad area, which is narrower than the Cu trace. Last, we spin coat the PI-2555 precursor 5 times on the Cu surface and cure it under 280℃ to make a planarized polyimide layer covering the Cu trace, as shown in Fig. 22(b). A well etched Cu pattern edge is shown in Fig. 23(a) and a finished 2-inch × 2-inch Cu layer is shown in Fig. 23(b).

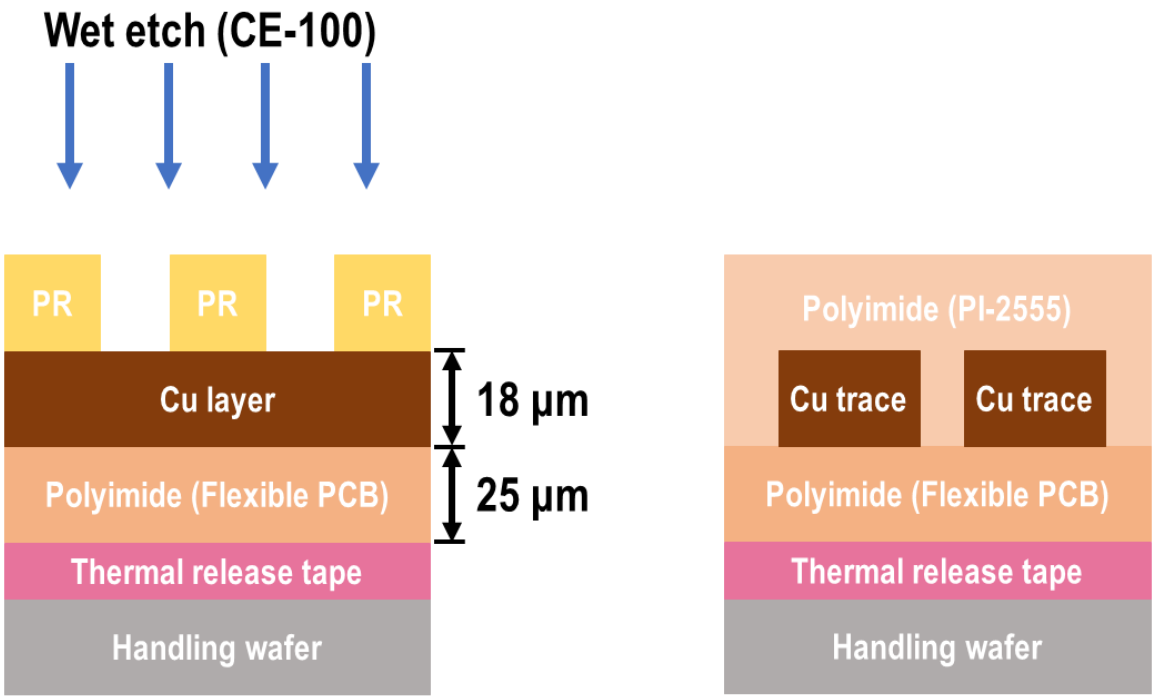

(a) (b)

Fig. 22 Schematic of Cu layer preparation step. The Cu trace pattern is made by (a) wet etch and (b) a planarized polyimide layer is coated on the top.

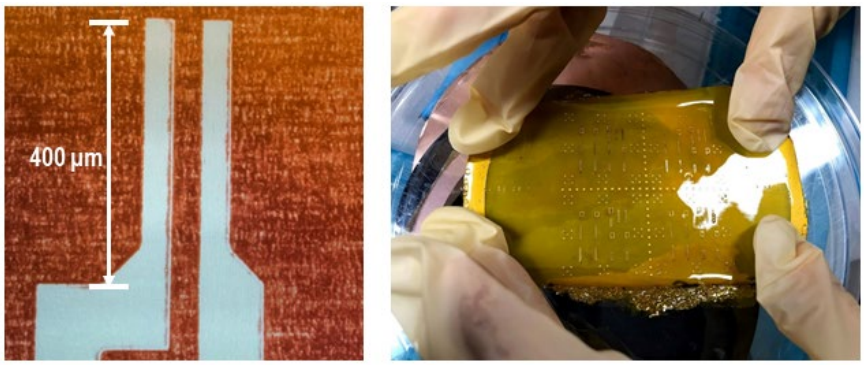

Fig. 23 (a) Microscopic image of the Cu trace (b) A finished 2-inch × 2-inch Cu layer.

4.2 Magnetic Core Preparation

The two magnetic core layers are designed to be above and below the Cu inductor traces, respectively. The 3 μm laminated (15×200 μm) CoZrTaB thin film is sputtered and used as the core material.

Preparation of substrate 1 (with Cu pattern) has been mentioned in the previous paragraph. Substrate 2 is prepared by coating PI-2555 on a handling wafer and curing it.

Then the magnetic core layer is made by a standard lift-off process. The nLOF 2070 negative photoresist is coated on both substrates at 1500 rpm to achieved 9 μm thickness. The lithography step is also finished by OAI 808 aligner. The schematics of two substrates prior to sputter is shown in Fig. 24.

The laminated CoZrTaB thin film is deposited and then we put them in the sonicator for 60 minutes to finish the lift-off process. The finished substrates pictures are shown in Fig. 25.

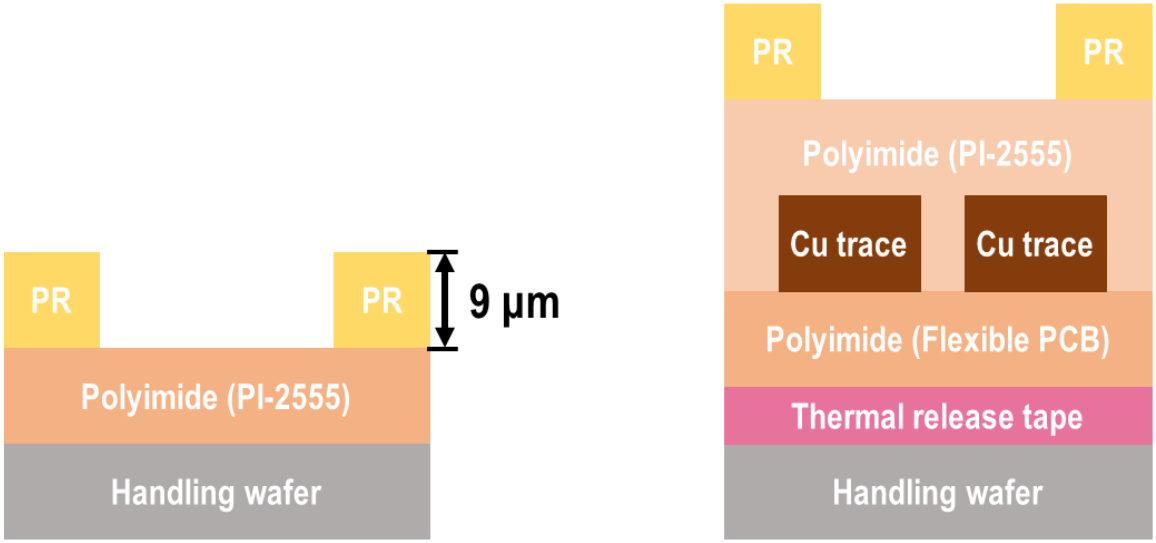

(a) (b)

Fig. 24 Schematic of two substrates with photoresist (a) Substrate 2 (b) Substrate 1.

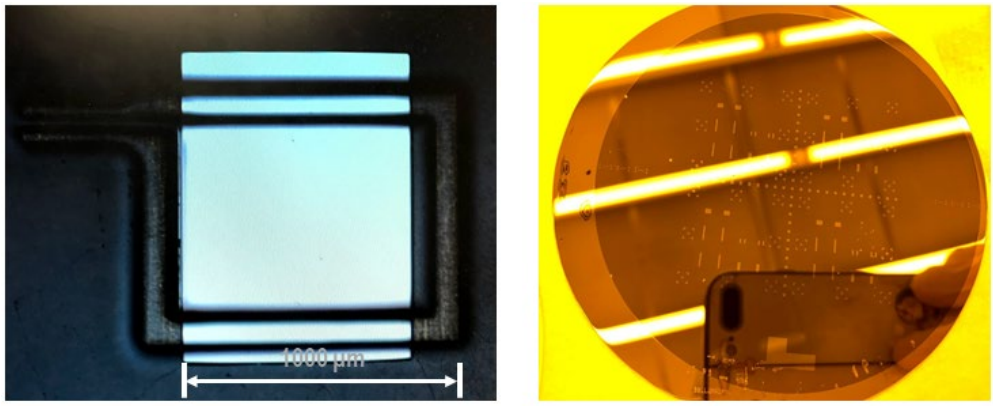

(a) (b)

Fig. 25 Two substrates with finished magnetic core. (a) Substrate 1 (b) Substrate 2. They are referring to the structure shown in upper part (with holding wafer still attached to the bottom) and the lower part of Fig. 26.

4.3 Final Assembly

The last step is to use the Finetech flipchip bonder to align and attach the two substrates: First, substrate 1 is removed from the original holding wafer, and then attached to another handling wafer on the top face. The handling wafer can protect the surface and enable a good attachment to the vacuum mount of the flip-chip bonder. Second, BCB-Cyclotene was spin-coated on substrate 2, which has a good adhesion with polyimide surface and the curing temperature is relatively low (250°C). Schematic of two substrates that are ready for bonding is shown in Fig. 26.

During the bonding process, the thermal and pressure were also provided by the flip-chip bonder. Last, one more lithography and dry etch is required to etch a small rectangle on the Cu contact pad with SF_6/Ar gas flow. The finished devices are shown in Fig. 27.

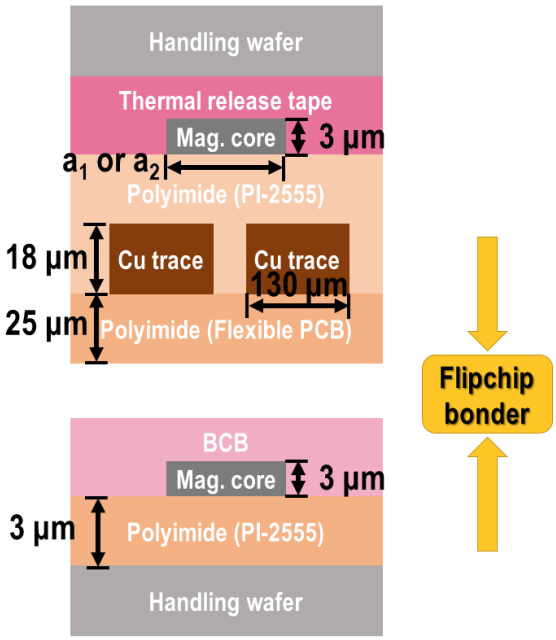

Fig. 26 Schematic of two substrates after bonding preparation is finished. The dimension of each part has been indicated in the plot. The width of magnetic core is described in 3.3.2.

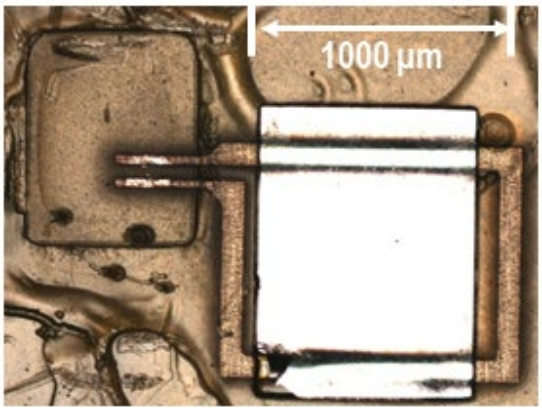

Fig. 27 Top view of a finished device (design 4 core 1) under microscope.

CHAPTER 5

DC/RF MEASUREMENT AND ANALYSIS

5.1 Measurement Platform Setup

5.1.1 DC Measurement

From the calculation results, we can see that the DCR of our devices is at $10^{-2}\sim10^{-1}\ \Omega$ level, which is equivalent to the contact resistance of our DC probe station. It is necessary to eliminate the effect of contact resistance and extract the DCR individually. Fig. 28 indicates the method we used to achieve this:

Step 1: Probe at the same side of the Cu trace. The two probe ends (probing points) are close but not contacted with each other. Measure the resistance value R_1. This value is supposed to be the contact resistance.

Step 2: Probe at the two sides of the Cu trace. Measure the resistance value R_2. This value has DCR and contact resistance. Then DCR can be expressed as:

$$\mathrm{DCR} = \mathrm{R}_2 - \mathrm{R}_1$$

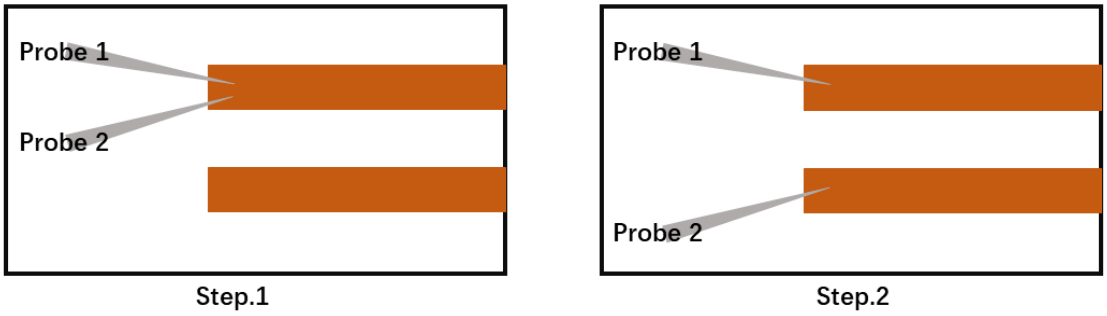

Fig. 28 Schematic of DC resistance measurement method. The brown part stands for Cu trace.

5.1.2 RF Measurement

Our RF measurement system is shown in Fig. 29. The hardware part consists of Cascade GS probe (110μm), Micromanipulator 6200 probe station, and Keysight E5071 network analyzer. For the data process part, Wincal software can measure the S parameter and generate s1p file. We used MATLAB to convert the data to inductance, AC resistance (ACR), and quality factor. The system was calibrated with the Cascade impedance standard substrates.

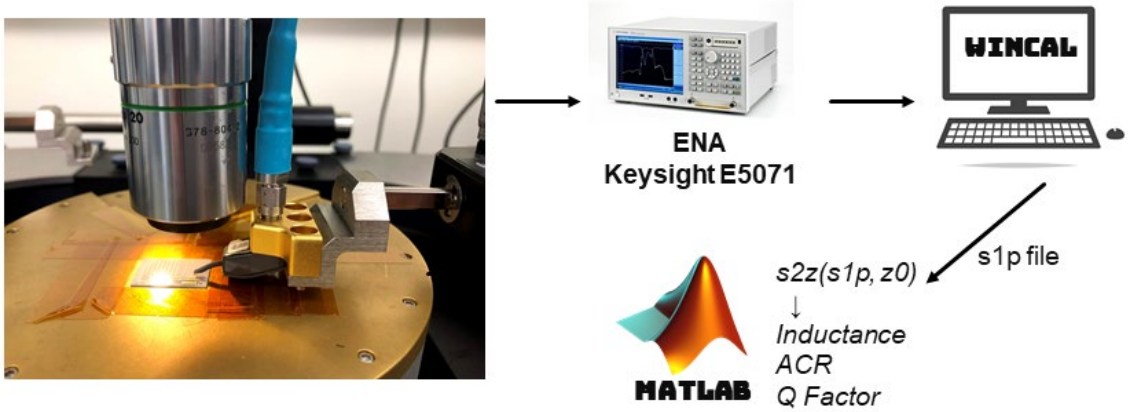

Fig. 29 Schematic of RF measurement system, including RF probe station, network analyzer, and data process software.

5.2 Measurement Results and Analysis

The DC measurement results of the design 1-4 are 67.4 mΩ, 58.3 mΩ, 49.8 mΩ, 47.1 mΩ. The RF measurement results of air core inductors and magnetic core inductors are shown in Fig. 30 and Fig. 31, respectively, with the corresponding dimension and pattern on the top right. Valid data cannot be measured from some of the magnetic core inductors because of fabrication yield, such as pattern loss or damage. The 100 MHz performance data is listed in Table 8 and Table 9.

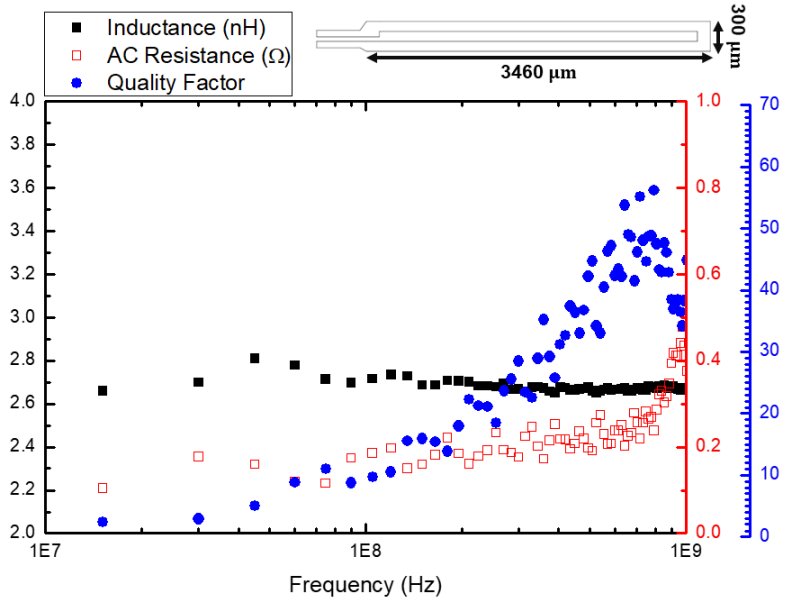
Inductance (nH)
AC Resistance (Ω)
Quality Factor
300 µm
3460 µm
4.0
3.8
3.6
3.4
3.2
3.0
2.8
2.6
2.4
2.2
2.0
1.0
0.8
0.6
0.4
0.2
0.0
70
60
50
40
30
20
10
0
1E7
1E8
1E9
Frequency (Hz)

(a)

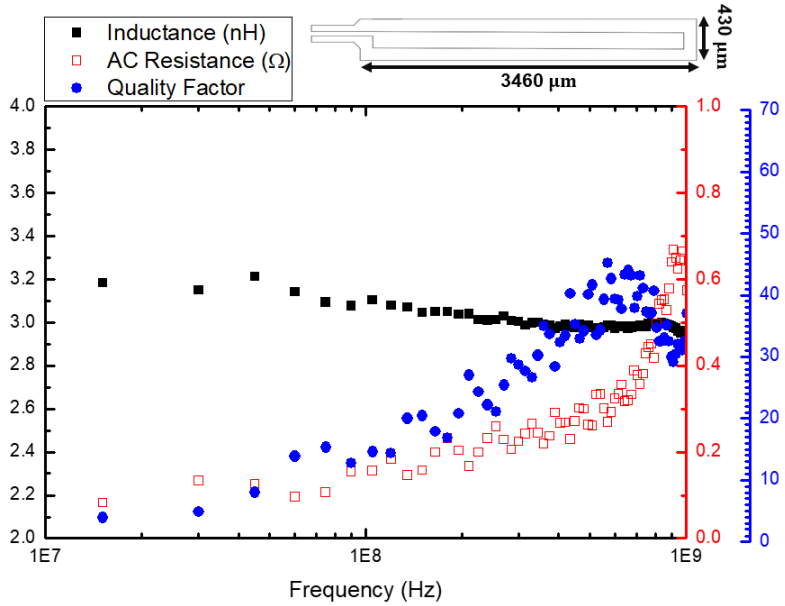
Inductance (nH)
AC Resistance (Ω)
Quality Factor
430 µm
3460 µm
4.0
3.8
3.6
3.4
3.2
3.0
2.8
2.6
2.4
2.2
2.0
1.0
0.8
0.6
0.4
0.2
0.0
70
60
50
40
30
20
10
0
1E7
1E8
1E9
Frequency (Hz)

(b)

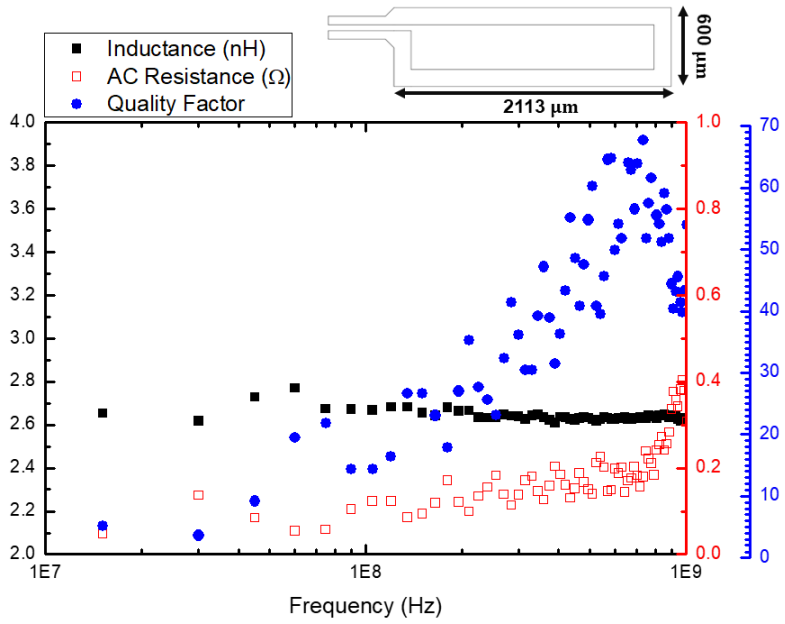

(c)

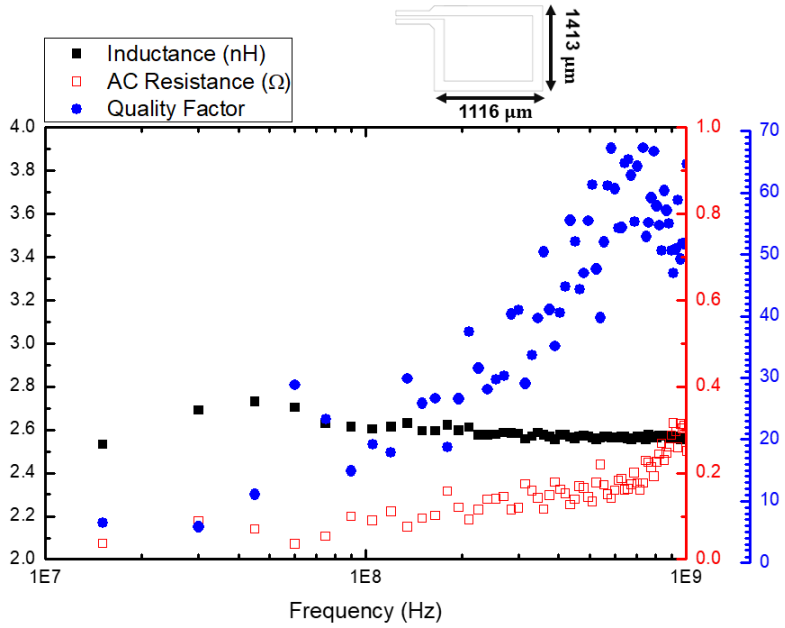

(d)

Fig. 30 RF measurement results of the air core inductors of (a) design 1 (b) design 2 (c) design 3 (d) design 4.

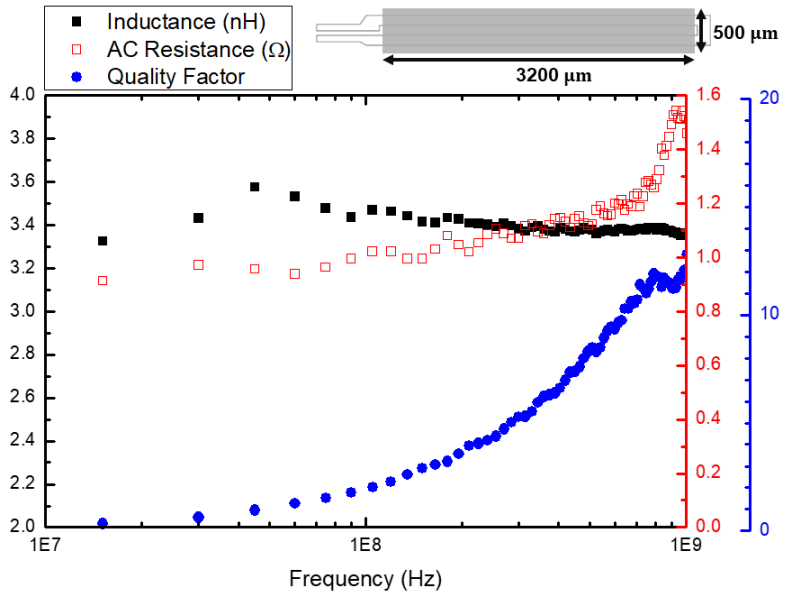
Inductance (nH)
AC Resistance (Ω)
Quality Factor
500 µm
3200 µm
4.0
3.8
3.6
3.4
3.2
3.0
2.8
2.6
2.4
2.2
2.0
1.6
1.4
1.2
1.0
0.8
0.6
0.4
0.2
0.0
20
10
0
1E7
1E8
1E9
Frequency (Hz)

(a)

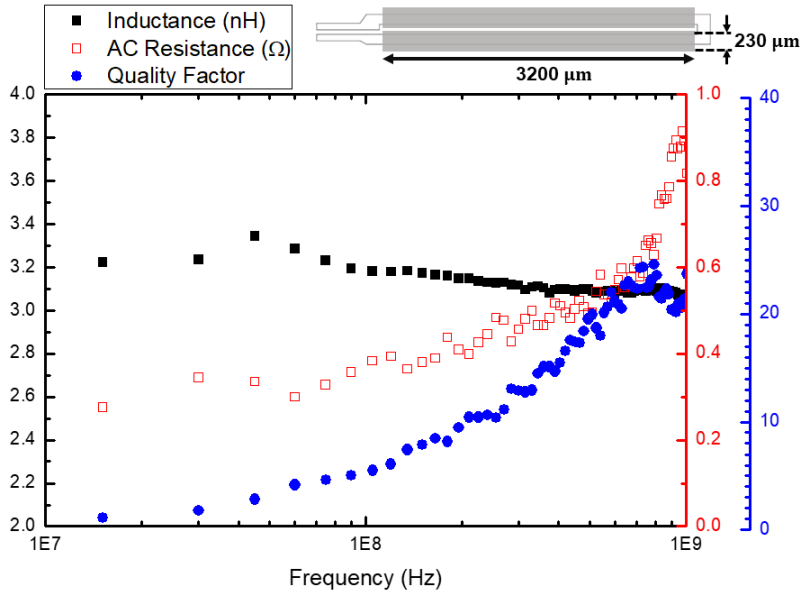
Inductance (nH)
AC Resistance (Ω)
Quality Factor
230 µm
3200 µm
4.0
3.8
3.6
3.4
3.2
3.0
2.8
2.6
2.4
2.2
2.0
1.0
0.8
0.6
0.4
0.2
0.0
40
30
20
10
0
1E7
1E8
1E9
Frequency (Hz)

(b)

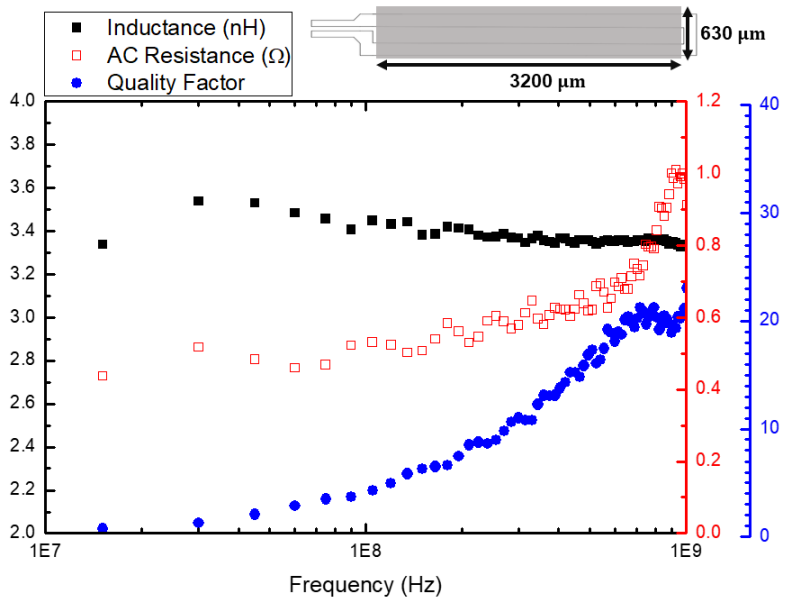
Inductance (nH)
AC Resistance (Ω)
Quality Factor
630 µm
3200 µm
4.0
3.8
3.6
3.4
3.2
3.0
2.8
2.6
2.4
2.2
2.0
1.2
1.0
0.8
0.6
0.4
0.2
0.0
40
30
20
10
0
1E7
1E8
1E9
Frequency (Hz)

(c)

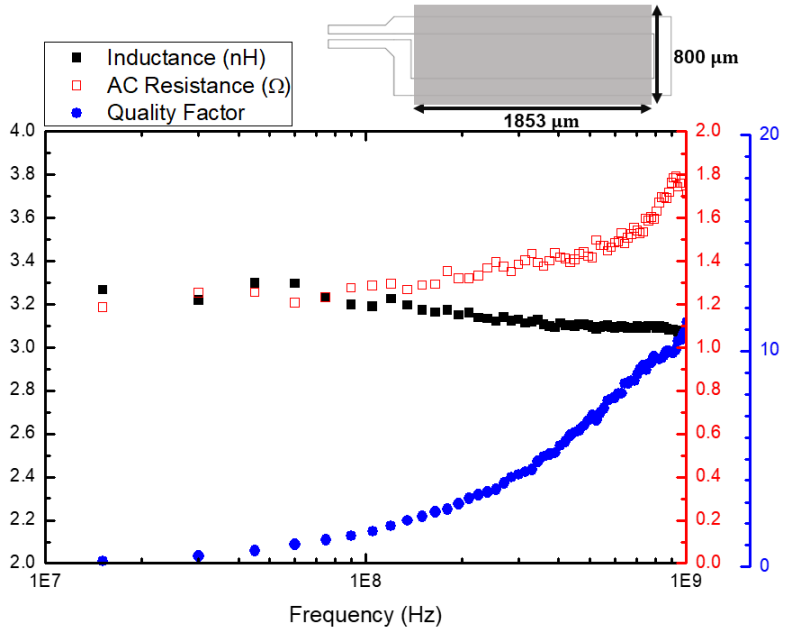
Inductance (nH)
AC Resistance (Ω)
Quality Factor
800 µm
1853 µm
4.0
3.8
3.6
3.4
3.2
3.0
2.8
2.6
2.4
2.2
2.0
2.0
1.8
1.6
1.4
1.2
1.0
0.8
0.6
0.4
0.2
0.0
20
10
0
1E7
1E8
1E9
Frequency (Hz)

(d)

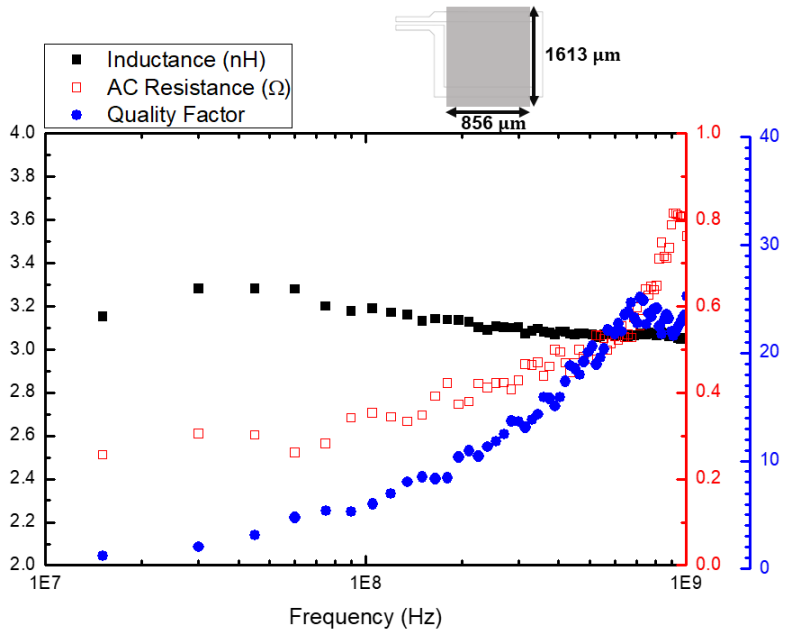

(e)

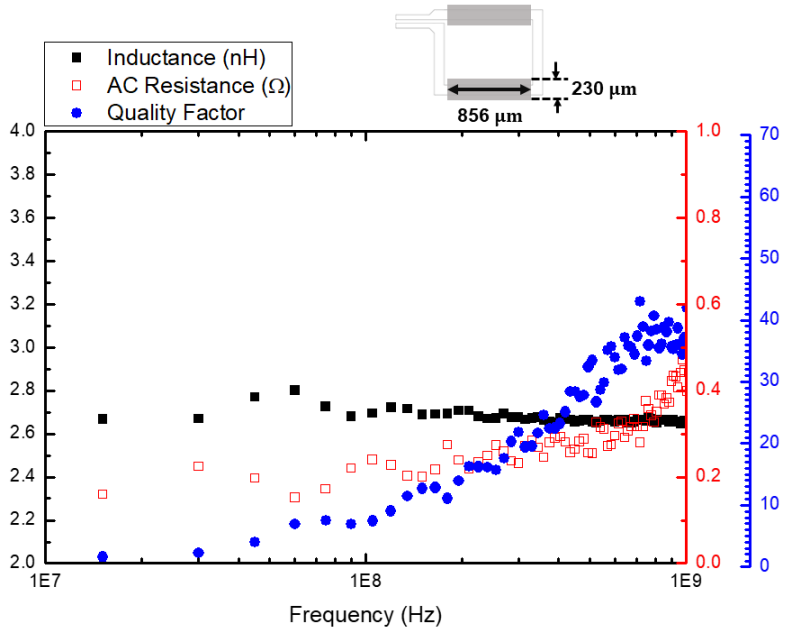

(f)

Fig. 31 RF measurement results of magnetic core inductors of (a) design 1 core 1 (b) design 1 core 2 (c) design 2 core 1 (d) design 3 core 1 (e) design 4 core 1 (f) design 4 core 2.

Table 8
Measurement and Simulation Results of Four Types of Cu Pattern of Air Core Pattern at 100 MHz Frequency

Design #	1	2	3	4
Inductance (nH) (Mes./Sim.)	2.81/2.95	3.08/3.12	2.67/2.41	2.57/2.37
ACR (Ω) (Mes./Sim.)	0.185/0.101	0.157/0.086	0.123/0.064	0.087/0.058
Quality factor (Mes./Sim.)	9.54/18.33	12.33/22.84	13.64/23.71	18.56/25.74

Table 9
Measurement Results of Four Types of Cu Pattern and Two Types of Magnetic Core Pattern at 100 MHz Frequency

Design #	1		2		3		4	
Core pattern #	1	2	1	2	1	2	1	2
Inductance (nH) (Mes./Sim.)	3.47/ 3.46	3.18/ 3.27	3.45/ 3.67	-	3.19/ 3.31	-	3.19/ 3.19	2.70/ 3.12
ACR (Ω) (Mes./Sim.)	1.055/ 0.296	0.383/ 0.243	0.531/ 0.339	-	1.285/ 0.231	-	0.352/ 0.203	0.240/ 0.189
Quality factor (Mes./Sim.)	2.07/ 7.34	5.49/ 8.46	4.28/ 6.8	-	1.64/ 9.00	-	5.98/ 9.87	7.42/ 10.37

5.2.1 Inductance

In general, compared with their corresponding air core inductor, core pattern 1 can bring 12.0%-24.1% (average is 19.78%) inductance enhancement for the 4 Cu trace patterns at 100 MHz. This is better than core pattern 2 which is 9.15% on average. This result aligns with the magnetic flux density distribution (B field) extracted by Ansys Maxwell, as shown in Fig. 32. The center portion (the subtraction portion of core pattern 2) of the magnetic core contributes to the total magnetization more or less, depending on the different patterns. In our design, this factor cannot be ignored, suggesting core pattern 1 has a greater benefit to the inductance.

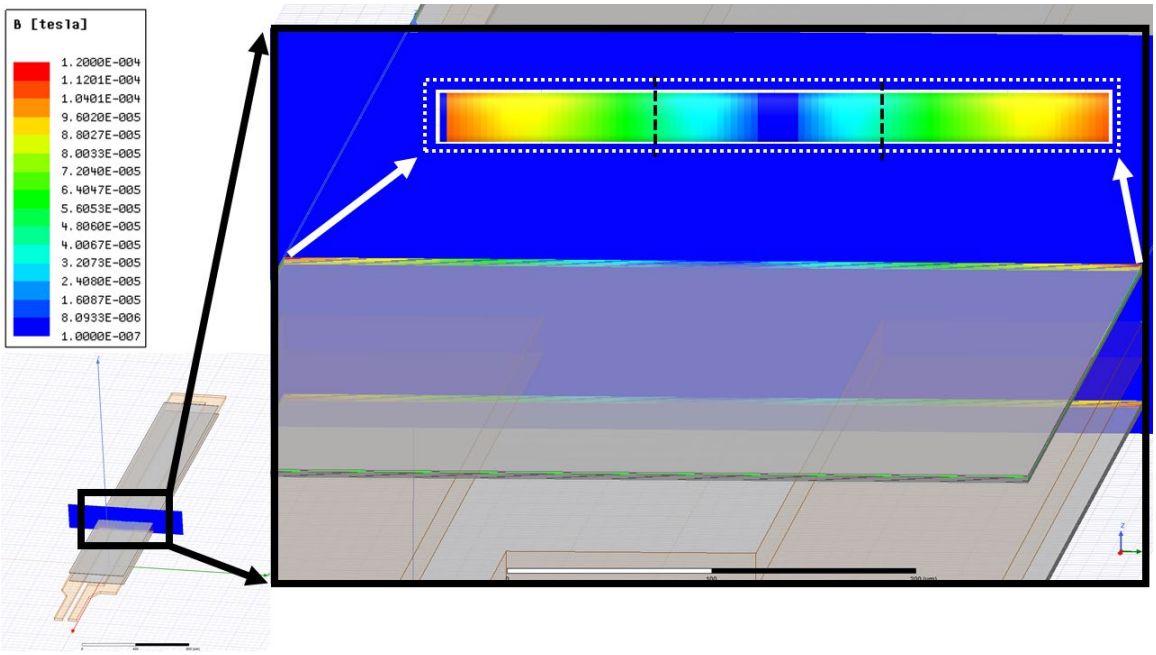

Fig. 32 B field distribution on the cross section of magnetic core extracted by Ansys Maxwell. The inset in the white dotted line show the B field magnitude at the intersecting line of the magnetic core top surface and the cross section plane.

Also, a discrepancy less than 10% can be seen between simulated and measured inductance in some designs, such as design 2-core pattern 1 and design 4-core pattern 2. This difference can be explained by two reasons:

(1) Error induced by the fabrication process. For example: the actual distance between Cu layer and core layer is larger than designed value, or the bonding process might create alignment offset, etc.

(2) The de facto M-H loop varying from the settings in the simulation. Some factors may be involved into this problem. Besides those factors discussed in chapter 2, another one that cannot be ignored is that the M-H loop was measured under low frequency (50 Hz). However, as the frequency extends to RF range, the M-H loop may change.[44-48]

The effective permeability is determined by the following equation[49]

$$\mu_{eff} = \frac{M_S}{H_{eff}} = \frac{M_S}{H_k + N_d M_S} = \frac{1}{\frac{H_k}{M_S} + N_d}$$

Where N_d is the demagnetization factor. As a result, the effective permeability is modulated by N_d and the ratio of H_k/M_s. For most of the ferromagnetic thin films, the demagnetization factor is strongly depending on their geometry, and the ration of thickness and horizontal dimensions; the demagnetization factor can be considered as “negligible” when this ration is small.[50] However, the demagnetization factor could be relatively expanding under some circumstances, such as multilayer/lamination profile or high substrate roughness, resulting from the coupling/interference between layers, or the special roughness profile [51, 52] A research[52] shows that a very thin Co on base Si shows low demagnetization factor, while this value will drastically increase on a “mound” surface, which has both

smoothening and roughening mechanisms. This is relatively similar to our magnetic thin film on the uneven or not perfectly planarized polyimide substrates.

All of inductance versus frequency curves are relatively stable, suggesting no ferromagnetic resonance happens within the measurement frequency range (< 1 GHz). This is consistent with our groups previous research output,[53] of which the high ferromagnetic resonant frequency (FMR) is larger than 1 GHz for CoZrTaB thin film. The FMR is expressed as:[49]

$$f_r = \frac{\gamma}{2\pi}\sqrt{\frac{M_s H_k}{\mu_0}}$$

Where γ is gyromagnetic ratio. The trade-off between f_r and H_k (or μ_{eff}) does not need to be considered within 1 GHz.

5.2.2 DC/AC Resistance

The measured DCR is slightly larger than calculated value due to narrower geometry of contact pad area. The measured values are still on the same level (below 100 mΩ), showing advantage to other topology types.

Generally, the ACRs of core pattern 1 inductors are larger than those of core pattern 2 inductors, especially for design 1. Here design 4 shows advantage of low ACRs with both of the core patterns. It can be seen, for all designs, 100 MHz is the ACR transition frequency. Beyond this point, ACRs begin to significantly increase.

5.2.3 Quality Factor

At 100 MHz, design 4-core pattern 2 achieves the highest quality factor of 7.42. The design with high inductance value does not have a good quality factor due its high ACR. The same reason leads to a remarkable quality factor loss compared with the simulation results.

The quality factor value grows as frequency increases to 0.9-1 GHz, of which the transition frequency is much higher than ACR, as the quality factor is calculated by:

$$Q = 2\pi f \frac{L}{ACR}$$

So, the quality factor can maintain increasing beyond 0.1 GHz though ACR surges.

5.3 Conclusion

We have demonstrated the CoZrTaB magnetic core successfully increases inductance value, which aligns with the simulation result. For those inductance-desired application, the large core area (core pattern 1) is more beneficial. We achieved 3.47 nH at 100 MHz and the device size is within 1.5 mm^2. Also, adding break or gap in the center portion of magnetic core can improve the quality factor. The ferromagnetic resonance was not detected, and the quality factor keeps increasing for the whole measurement frequency range, enabling capability to extending the working to GHz level.

CHAPTER 6

CONCLUSION

A comprehensive study of CoZrTaB thin film optimization, magnetic core inductor design, device fabrication and measurement/verification has been discussed. In the magnetic thin film part, the best deposition recipe (6 mTorr sputter pressure, lamination structure with SiO2 insulator, PI-2555 polyimide precursor) has been confirmed and the B-H loop parameters prove to be aligned with application requirement. Coercivity of 1.4 Oe and anisotropy field of 26.2 Oe have been obtained from a 4×100 nm CoZrTaB thin film on polyimide substrate. Prior to the design and optimization of magnetic core inductors, the B-H loop is imported into the Ansys Maxwell software to improve the simulation accuracy. Assisted with this software, inductance, AC resistance, and quality factor have been extracted for four types of Cu trace pattern with 2 kinds of magnetic core pattern. Also, the lamination profile (15 × 200 nm) has been confirmed to have the best inductance-ACR trade-off at 100 MHz.

In the experiment part, we fabricated the device in according to the designs that have been analyzed in the simulation. The magnetic core inductors are fabricated on polyimide substrate and, of which Cu trace pattern is made from wet etch on flexible PCB and the final assembly is finished by flipchip bonder. The following measurement results show that one of the magnetic core inductor design has low DCR (< 60 $m\Omega$), low ACR (0.531 Ω), and high inductance (3.45 nH) at 100 MHz. Considering its low profile (thickness < 200 μm) and small size (< 1.5 mm^2), it is a good candidate to be the passive component of power delivery module in low power consumption ICs. In addition, the fact that the device

is fabricated on polyimide substrates guarantees a wide range of packaging formfactor into which this inductor design can be integrated.

REFERENCES

[1] E. A. Burton *et al.*, "FIVR—Fully integrated voltage regulators on 4th generation Intel® Core™ SoCs," in *2014 IEEE Applied Power Electronics Conference and Exposition-APEC 2014*, 2014: IEEE, pp. 432-439.

[2] M. Sankarasubramanian *et al.*, "Magnetic Inductor Arrays for Intel® Fully Integrated Voltage Regulator (FIVR) on 10 th generation Intel® Core™ SoCs," in *2020 IEEE 70th Electronic Components and Technology Conference (ECTC)*, 2020: IEEE, pp. 399-404.

[3] K. Bharath *et al.*, "Integrated Voltage Regulator Efficiency Improvement using Coaxial Magnetic Composite Core Inductors," in *2021 IEEE 71st Electronic Components and Technology Conference (ECTC)*, 2021: IEEE, pp. 1286-1292.

[4] Y. Yang, L. Dorn-Gomba, R. Rodriguez, C. Mak, and A. Emadi, "Automotive power module packaging: current status and future trends," *IEEE Access,* vol. 8, pp. 160126-160144, 2020.

[5] R. Alizadeh and H. A. Mantooth, "A Review of Architectural Design and System Compatibility of Power Modules and Their Impacts on Power Electronics Systems," *IEEE Transactions on Power Electronics,* 2021.

[6] V. Issakov *et al.*, "Co-simulation and co-design of chip-package-board interfaces in highly-integrated RF systems," in *2016 IEEE Bipolar/BiCMOS Circuits and Technology Meeting (BCTM)*, 2016: IEEE, pp. 94-101.

[7] Y. Wu, I.-C. Yeng, and H. Yu, "The improvement of CoZrTaB thin films on different substrates for flexible device applications," *AIP Advances,* vol. 11, no. 2, p. 025139, 2021.

[8] N. Sturcken *et al.*, "Magnetic thin-film inductors for monolithic integration with CMOS," in *2015 IEEE International Electron Devices Meeting (IEDM)*, 2015: IEEE, pp. 11.4. 1-11.4. 4.

[9] S. Peng, J. Yu, C. Feeney, T. Ye, Z. Zhang, and N. Wang, "A micro-inductor with thin film magnetic core for a 20 MHz buck converter," *Journal of Magnetism and Magnetic Materials,* vol. 524, p. 167661, 2021.

[10] R. Meere, N. Wang, T. O'Donnell, S. Kulkarni, S. Roy, and S. C. O'Mathuna, "Magnetic-core and air-core inductors on silicon: A performance comparison up to 100 MHz," *IEEE transactions on magnetics,* vol. 47, no. 10, pp. 4429-4432, 2011.

[11] D. W. Lee, K.-P. Hwang, and S. X. Wang, "Fabrication and analysis of high-performance integrated solenoid inductor with magnetic core," *IEEE Transactions on Magnetics,* vol. 44, no. 11, pp. 4089-4095, 2008.

[12] H. T. Le *et al.*, "High-Q three-dimensional microfabricated magnetic-core toroidal inductors for power supplies in package," *IEEE Transactions on power electronics,* vol. 34, no. 1, pp. 74-85, 2018.

[13] W. Xu *et al.*, "Performance enhancement of on-chip inductors with permalloy magnetic rings," *IEEE Electron Device Letters,* vol. 32, no. 1, pp. 69-71, 2010.

[14] S. S. Boon, D. H. S. Wee, R. Salahuddin, and R. P. Singh, "Magnetic inductor integration in FO-WLP using RDL-first approach," in *2019 IEEE 21st Electronics Packaging Technology Conference (EPTC)*, 2019: IEEE, pp. 18-22.

[15] M. Khdour, H. Wu, and H. Yu, "High DC current density on-chip strip-line inductors integrated with magnetic film," *IEEE Transactions on Magnetics,* vol. 52, no. 7, pp. 1-4, 2016.

[16] T. Yang *et al.*, "Realization of High Electrical Performance On-chip Thick Copper Inductor Package by Via Interface Process Improvement for Metal Contact," in *2018 IEEE 68th Electronic Components and Technology Conference (ECTC)*, 2018: IEEE, pp. 1698-1705.

[17] S. Müller, M. L. F. Bellaredj, A. K. Davis, P. A. Kohl, and M. Swaminathan, "Design exploration of package-embedded inductors for high-efficiency integrated voltage regulators," *IEEE Transactions on Components, Packaging and Manufacturing Technology,* vol. 9, no. 1, pp. 96-106, 2018.

[18] J. T. Doyle, J. C. Stiff, S. Kulkarni, and A. Yildiz, "A low cost 100 MHz 2-Stage PSiP and evolution to a co-packaged/fully-integrated voltage regulator for SoC power delivery," in *2019 IEEE Custom Integrated Circuits Conference (CICC)*, 2019: IEEE, pp. 1-8.

[19] N. Sturcken *et al.*, "A 2.5 D integrated voltage regulator using coupled-magnetic-core inductors on silicon interposer," *IEEE Journal of solid-state circuits,* vol. 48, no. 1, pp. 244-254, 2012.

[20] H. K. Krishnamurthy *et al.*, "A digitally controlled fully integrated voltage regulator with 3D-TSV based on-die solenoid inductor with backside planar magnetic core in 14nm tri-gate CMOS," in *2017 Symposium on VLSI Technology*, 2017: IEEE, pp. C148-C149.

[21] H. Wu, D. S. Gardner, W. Xu, and H. Yu, "Integrated RF on-chip inductors with patterned Co-Zr-Ta-B films," *IEEE transactions on magnetics,* vol. 48, no. 11, pp. 4123-4126, 2012.

[22] H. Wu, M. Khdour, P. Apsangi, and H. Yu, "High-frequency magnetic thin-film inductor integrated on flexible organic substrates," *IEEE Transactions on Magnetics,* vol. 53, no. 11, pp. 1-7, 2017.

[23] W. H. Hayt Jr, J. A. Buck, and M. J. Akhtar, *Engineering Electromagnetics| (SIE)*. McGraw-Hill Education, 2020.

[24] C. Kittel, P. McEuen, and P. McEuen, *Introduction to solid state physics*. Wiley New York, 1996.

[25] D. S. Chuang, "Magnetic anisotrophy in ultrathin epitaxial films grown on surfaces vicinal to Cu (001)," Massachusetts Institute of Technology, 1994.

[26] R. Harris and D. Zobin, "The random anisotropy model for amorphous metallic alloys: generalized molecular field calculations," *Journal of Physics F: Metal Physics,* vol. 7, no. 2, p. 337, 1977.

[27] R. Alben, J. Becker, and M. Chi, "Random anisotropy in amorphous ferromagnets," *Journal of applied physics,* vol. 49, no. 3, pp. 1653-1658, 1978.

[28] A. Neudert, J. McCord, R. Schäfer, and L. Schultz, "Dynamic anisotropy in amorphous CoZrTa films," *Journal of applied physics,* vol. 95, no. 11, pp. 6595-6597, 2004.

[29] R. A. Serway and J. W. Jewett, *Principles of physics*. Saunders College Pub. Fort Worth, TX, 1998.

[30] B. D. Cullity and C. D. Graham, *Introduction to magnetic materials*. John Wiley & Sons, 2011.

[31] K. Koh, D. S. Gardner, C. Yang, K. P. O'brien, N. Tayebi, and L. Lin, "High frequency microwave on-chip inductors using increased ferromagnetic resonance frequency of magnetic films," in *2015 28th IEEE International Conference on Micro Electro Mechanical Systems (MEMS)*, 2015: IEEE, pp. 208-211.

[32] D. S. Gardner *et al.*, "Integrated on-chip inductors with magnetic films," in *2006 International Electron Devices Meeting*, 2006: IEEE, pp. 1-4.

[33] D. Lordan, G. Wei, P. McCloskey, C. O'Mathuna, and A. Masood, "Origin of perpendicular magnetic anisotropy in amorphous thin films," *Scientific Reports,* vol. 11, no. 1, pp. 1-12, 2021.

[34] A. Aharoni, *Introduction to the Theory of Ferromagnetism*. Clarendon Press, 2000.

[35] H. Kronmüller, K.-D. Durst, and M. Sagawa, "Analysis of the magnetic hardening mechanism in RE-FeB permanent magnets," *Journal of Magnetism and Magnetic Materials,* vol. 74, no. 3, pp. 291-302, 1988.

[36] L. Tauxe, H. N. Bertram, and C. Seberino, "Physical interpretation of hysteresis loops: Micromagnetic modeling of fine particle magnetite," *Geochemistry, Geophysics, Geosystems,* vol. 3, no. 10, pp. 1-22, 2002.

[37] C. R. Pike, A. P. Roberts, M. J. Dekkers, and K. L. Verosub, "An investigation of multi-domain hysteresis mechanisms using FORC diagrams," *Physics of the Earth and Planetary Interiors,* vol. 126, no. 1-2, pp. 11-25, 2001.

[38] T. Dastagir, W. Xu, S. Sinha, H. Wu, Y. Cao, and H. Yu, "Tuning the permeability of permalloy films for on-chip inductor applications," *Applied Physics Letters,* vol. 97, no. 16, p. 162506, 2010.

[39] C. Lian, L. Tian-Quan, S. Pu-Nan, and X. Hui-Jie, "The hysteresis loops of a ferroelectric bilayer film with surface transition layers," *Chinese Physics B,* vol. 19, no. 7, p. 077701, 2010.

[40] P. Rasilo *et al.*, "Modeling of hysteresis losses in ferromagnetic laminations under mechanical stress," *IEEE Transactions on Magnetics,* vol. 52, no. 3, pp. 1-4, 2015.

[41] J. Becker, "Surface effects of hysteresis loop shapes in high-coercive-force crystallized amorphous alloys," *IEEE Transactions on Magnetics,* vol. 18, no. 6, pp. 1451-1453, 1982.

[42] X. Tao, V. Koncar, T.-H. Huang, C.-L. Shen, Y.-C. Ko, and G.-T. Jou, "How to make reliable, washable, and wearable textronic devices," *Sensors,* vol. 17, no. 4, p. 673, 2017.

[43] A. Petropoulos, D. N. Pagonis, and G. Kaltsas, "Flexible PCB-MEMS flow sensor," *Procedia Engineering,* vol. 47, pp. 236-239, 2012.

[44] A. El-Ghazaly, R. White, and S. Wang, "Increasing ferromagnetic resonance frequency using lamination and shape," *Journal of Applied Physics,* vol. 117, no. 17, p. 17E502, 2015.

[45] D. Zhmetko, Y. N. Troschenkov, and A. Matsura, "The frequency dependence of demagnetizing factor of a Fe-based amorphous ribbon," *Journal of magnetism and magnetic materials,* vol. 324, no. 17, pp. 2609-2612, 2012.

[46] M. Arya, M. N. Gandhi, S. S. Prabhu, V. G. Achanta, and S. P. Duttagupta, "Nickel-cobalt-zinc ferrite nanoparticles for radio-frequency/terahertz frequency-selective surface application," *IET Nanodielectrics,* vol. 4, no. 3, pp. 98-106, 2021.

[47] I. Morales *et al.*, "High frequency hysteresis losses on γ-Fe2O3 and Fe3O4: Susceptibility as a magnetic stamp for chain formation," *Nanomaterials,* vol. 8, no. 12, p. 970, 2018.

[48] Y. S. Kivshar, O. H. Olsen, and M. R. Samuelsen, "Hysteresis loop induced by rf radiation in Josephson junctions: an analytical approach," *Physics Letters A,* vol. 168, no. 5-6, pp. 391-399, 1992.

[49] C. Kittel, "On the theory of ferromagnetic resonance absorption," *Physical review,* vol. 73, no. 2, p. 155, 1948.

[50] C. Kittel, "Theory of the structure of ferromagnetic domains in films and small particles," *Physical Review,* vol. 70, no. 11-12, p. 965, 1946.

[51] V. Loyau, A. Aubert, M. LoBue, and F. Mazaleyrat, "Analytical modeling of demagnetizing effect in magnetoelectric ferrite/PZT/ferrite trilayers taking into account a mechanical coupling," *Journal of Magnetism and Magnetic Materials,* vol. 426, pp. 530-539, 2017.

[52] Y.-P. Zhao, G. Palasantzas, G.-C. Wang, and J. T. M. De Hosson, "Surface/interface-roughness-induced demagnetizing effect in thin magnetic films," *Physical Review B,* vol. 60, no. 2, p. 1216, 1999.

[53] H. Wu, *Integrated Inductors with Micro-Patterned Magnetic Thin Films for RF and Power Applications*. Arizona State University, 2013.